

Phenotypic differences between interfertile *Chlamydomonas* species

We're crossing *C. reinhardtii* and *C. smithii* algae for high-throughput genotype-phenotype mapping. In preparation, we're comparing the parents to uncover unique species-specific phenotypes.

Contributors (A-Z)

Prachee Avasthi, Brae M. Bigge, Ben Braverman, Feridun Mert Celebi, Tara Essock-Burns, Megan L. Hochstrasser, Galo Garcia III, Cameron Dale MacQuarrie, David Q. Matus, David G. Mets, Taylor Reiter, Harper Wood, Ryan York

Version 7 · Mar 31, 2025

Purpose

We're working to understand the associations between genotypes and phenotypes across the tree of life. Analyzing variation among interbreeding populations is a powerful tool for dissecting genotype-phenotype relationships.

To build our framework from the bottom up, we're starting by breeding interfertile *Chlamydomonas* species – *C. reinhardtii* and *C. smithii* – and performing high-dimensional characterization of many aspects of their biology. Here, we describe multiple phenotypes for each of the two parental species. These phenotypes will serve

as a baseline against which we will compare phenotypic and genotypic differences in the progeny of the hybridized species.

So far, we've studied the two species' environmental adaptations, sensitivity to lysis by detergent, cell wall morphology, gross cell morphology, and motility patterns. We've shared the data as we collected and analyzed it, and this pub contains the bulk of this work. If we add new phenotypic data going forward, it will appear in new pubs.

- This pub is part of the **platform effort**, "[Genetics: Decoding evolutionary drivers across biology](#)." Visit the platform narrative for more background and context.
- Our **Fiji macro**, **CellProfiler pipeline**, and **code** in R and Python are available in [this GitHub repository](#).
- Our **calcofluor-white-stained microscopy data** are available on [Zenodo](#).
- Our **focus-filtered time-lapse data and measurements** are available on [Zenodo](#).
- Our **high-resolution confocal z-stacks** for visualizing organelle morphology are available on [Zenodo](#).
- You can find a step-by-step **protocol** on [immobilizing cells for live imaging](#) on protocols.io.

Background and goals

We are advancing an initiative to [understand how genes and environments interact to drive variation in organismal traits](#). To investigate the relationship between genotypes and phenotypes, we need a population with both genetic and phenotypic diversity. A traditional solution would be to perform mutagenesis in an otherwise isogenic population, and then isolate individual alleles. While useful, the genetic changes that result from mutagenesis are fundamentally different from the forms of genetic variation that drive phenotypic variation in an actively interbreeding natural population. Such an approach also won't allow us to look at variation driven by specific allele combinations. A powerful alternative is to study the relationship between genotypic and phenotypic variation within a naturally varying population, as is done with experiments such as quantitative trait locus (QTL) mapping [\[1\]](#).

We chose to create a diverse population by hybridizing two interfertile species. We selected *Chlamydomonas reinhardtii* and *Chlamydomonas smithii* because they produce viable progeny when mated [2][3], are easy to maintain in clonal cultures, and, being unicellular algae, offer the potential to perform a variety of high-throughput analyses. However, little is known about the aspects of biology that differentiate these species (see Table 1). Given this, we compared a variety of phenotypes among these parent species to identify key axes of variation between them. These analyses will act as priors for all downstream comparisons of their progeny.

Brief background on *Chlamydomonas reinhardtii* and *smithii* species

C. reinhardtii is widely used as a model to study cellular processes like photosynthesis, cilia formation, and cell division [4]. *C. smithii* is less well characterized, even though these two species share a similar history [5][6]. In fact, the cells we used in this study were propagated from cultures isolated from soil fields in Massachusetts in 1945. For more than seven decades, both species have been subcultured under laboratory conditions, implying that any apparent differences between the species shouldn't stem from disparate lab adaptations, since they have been exposed to similar levels of adaptation opportunities.

To date, several genotypic differences have been observed between these two species including differences in their nuclear, chloroplast, and mitochondrial genomes [7][8][9][10][11], but a quality reference genome for *C. smithii* does not yet exist. Phenotypic differences are less well characterized – we've summarized the few previously reported differences in Table 1. The dearth of studies on *C. smithii* has led some to mischaracterize the species as a wild-type *C. reinhardtii* strain. For instance, *C. smithii* was recently used as a baseline wild-type *C. reinhardtii* strain in a comparison with *C. reinhardtii* cell wall mutants [12] and has been referred to as a *C. reinhardtii* field strain even though it has been subcultured in labs for the same amount of time as bona fide *C. reinhardtii* lab strains [7].

Phenotype	<i>C. reinhardtii</i>	<i>C. smithii</i>
Doubling time in the dark [13]	~24–31 hours	~72–108 hours
Cell volume [13]	110–115 μm^3	100 μm^3
Nuclear volume [13]	9.5–10.3 μm^3	11 μm^3
Morphology	10 μm long [14] 3 μm wide [14] ~6.5 μm diameter [7]	7.5–11 μm long [3] 3–7.5 μm wide [3] ~7.5 μm diameter [7]
Chlorophyll content [7]	~1600–2100 APC-A intensity	~1800 APC-A intensity
Heterotrophic growth [7]	~0.09–0.27 omnilog units	~0.92 omnilog units
Phototrophic growth [7]	–	~0.003 $\Delta\text{OD}_{680}/\text{h}$

Table 1

Previously reported phenotypic differences between the two *Chlamydomonas* species we’re studying.

The approach

Before isolating *C. reinhardtii* × *C. smithii* hybrid strains, it is important that we understand the baseline differences between these two species. We’ve investigated specific traits in these organisms that we can efficiently adapt to high-throughput methods, align with our research goals, and take advantage of our in-house tools and expertise. We’ve used both single-cell and multi-cell analyses to differentiate these species. These findings will provide the foundation for upcoming experiments to map associations between genotypes and phenotypes.

Here, we describe phenotypes that we’ve observed for these two *Chlamydomonas* species. First, we observed their growth under various culture conditions, altering nutrients, illumination, and temperature. We used two *C. reinhardtii* strains of opposing mating types in this initial study to determine if these phenotypes were mating-type dependent; however, we only used one *C. smithii* strain because a mating type pair of this species is not yet accessible through culture collection centers. We chose which growth media to use in this study based on in-house availability and variability of

nutrients. We also grew these cells on media supplemented with various antibiotics and fungicides to observe their response to these stresses. Next, we treated cells with a low-concentration detergent to test resistance to lysis and compared cell wall traits between these species. We also did a thorough analysis of the two-dimensional gross morphology and motility patterns of each species. Finally, we established a live imaging workflow to obtain high-resolution images to visualize the three-dimensional structure of organelle morphology.

Our **Fiji macro**, **CellProfiler pipeline**, and **code** in R and Python are available in this [GitHub repository](https://doi.org/10.5281/zenodo.10152769) (DOI: [10.5281/zenodo.10152769](https://doi.org/10.5281/zenodo.10152769)).

Species and strains

Species	Strain numbers and source links	Mating type	Site of parent isolation	Phenotype
<i>Chlamydomonas reinhardtii</i>	137c, cc-124, UTEX2243, SAG 33.89 (source)	(-)	<ul style="list-style-type: none"> • Amherst, Massachusetts, USA • Potato field soil • 1945 	Wild-type
<i>Chlamydomonas reinhardtii</i>	137c, cc-125, UTEX2244, SAG 34.89 (source)	(+)	<ul style="list-style-type: none"> • Amherst, Massachusetts, USA • Potato field soil • 1945 	Wild-type
<i>Chlamydomonas smithii</i>	136f, cc-1373, UTEX1062, SAG 54.72 (source)	(+)	<ul style="list-style-type: none"> • South Deerfield, Massachusetts, USA • Tobacco field soil • 1945 	Wild-type
<i>Chlamydomonas reinhardtii</i>	cc-1731, cw2 (source)	(+)	Not isolated from an environmental source – derived from 137c [15]	Cell wall-deficient

Table 2

Organisms used in this pub.

We ordered all species from the Chlamydomonas Resource Center.

Cell maintenance

After receiving strains from the culture center (Table 2), we streaked cells out to individual colonies on TAP media with 1.5% agar. We cultured cells from single colonies in liquid TAP media (UTEX) and then seeded them onto plates of TAP media with 1.5% agar to form a confluent lawn either at 24 °C under constant illumination or at ambient temperature under 12:12-hour light:dark cycles. For the 24 °C condition, we maintained cells in an incubator (internal dimensions 84 × 46 × 33 cm) equipped with five dimmable LED strips emitting across the red and blue spectrum (460 nm–620 nm). Our light meter read the luminosity ranging from 500–3,300 lux in this enclosed environment. We grew cells at ambient temperature on an open bench equipped with three GE Full Balanced Spectrum 9 Watt BR30 LED bulbs installed in clamp lamps. Our light meter read the luminosity at 1,400–2,500 lux in this area.

Extracting data displayed in Table 1

For the chlorophyll content, heterotrophic growth, and phototrophic growth data in Table 1, we extracted raw values from published bar graphs [7] using the WebPlotDigitizer tool [16].

Media components

We made all solid media with 1.5% agar. We made “water” plates with ultrapure water from a Milli-Q EQ 7008 system equipped with a 0.22 µm filter. Individual media components are as follows:

TAP (tris-acetate-phosphate) media

375 µM NH₄Cl, 17.5 µM CaCl₂*2H₂O, 20 µM MgSO₄*7H₂O, 6 µM Na₂HPO₄, 4 µM KH₂PO₄, 200 µM Trizma base, 170 µM glacial acetic acid, 0.1% v/v of Hunter’s trace elements solution (134 µM Na₂EDTA*2H₂O, 770 µM ZnSO₄*7H₂O, 184 µM H₃BO₃, 26 µM MnCl₂*4H₂O, 18 µM FeSO₄*7H₂O, 7 µM CoCl₂*6H₂O, 5 µM CuSO₄*5H₂O, and 800 nM (NH₄)₆Mo₇O₂₄*4H₂O). Suspended in ultrapure water. We purchased complete liquid media from UTEX. We supplemented media with 50–500 µM calcofluor-white

(Fluorescent Brightener 28), 250 μM Congo red, 100–500 $\mu\text{g}/\text{mL}$ ampicillin, 100 $\mu\text{g}/\text{mL}$ cefotaxime, 40 $\mu\text{g}/\text{mL}$ carbendazim, and/or 50 $\mu\text{g}/\text{mL}$ Zeocin, where noted.

Soil extract media

96% Bristol media and 4% pasteurized soil water supernatant (0.05 mM CaCO_3 , 2.5% greenhouse soil, suspended in ultrapure water). We purchased complete liquid media from UTEX.

Bristol media

2.94 mM NaNO_3 , 0.17 mM $\text{CaCl}_2 \cdot 2\text{H}_2\text{O}$, 0.3 mM $\text{MgSO}_4 \cdot 7\text{H}_2\text{O}$, 0.43 mM K_2HPO_4 , 1.29 mM KH_2PO_4 , and 0.43 mM NaCl . Suspended in ultrapure fresh water. We purchased complete liquid media from UTEX.

Kuhl's media

10 mM KNO_3 , 4.5 mM $\text{NaH}_2\text{PO}_4 \cdot \text{H}_2\text{O}$, 0.5 mM $\text{Na}_2\text{HPO}_4 \cdot 2\text{H}_2\text{O}$, 1 mM $\text{MgSO}_4 \cdot 7\text{H}_2\text{O}$, 0.1 mM $\text{CaCl}_3 \cdot 2\text{H}_2\text{O}$, 24.8 μM $\text{FeSO}_4 \cdot 7\text{H}_2\text{O}$, 25 μM Na_2EDTA , 987 nM H_3BO_3 , 1 μM $\text{MnSO}_4 \cdot \text{H}_2\text{O}$, 1 μM $\text{ZnSO}_4 \cdot 7\text{H}_2\text{O}$, 10 nM $\text{CuSO}_4 \cdot 5\text{H}_2\text{O}$, 10 nM $(\text{NH}_4)_6\text{Mo}_7\text{O}_{24} \cdot 4\text{H}_2\text{O}$. Suspended in ultrapure water.

K media

882 μM NaNO_3 , 50 μM NH_4Cl , 10 μM Na_2 b-glycerophosphate, 504 μM $\text{Na}_2\text{SiO}_3 \cdot 9\text{H}_2\text{O}$, 10 nM H_2SeO_3 , 1 mM tris base (pH 7.2), 111 μM $\text{Na}_2\text{EDTA} \cdot 2\text{H}_2\text{O}$, 12 μM $\text{FeCl}_3 \cdot 6\text{H}_2\text{O}$, 900 nM $\text{MnCl}_2 \cdot 4\text{H}_2\text{O}$, 80 nM $\text{ZnSO}_4 \cdot 7\text{H}_2\text{O}$, 42 nM $\text{CoCl}_2 \cdot 6\text{H}_2\text{O}$, 26 nM $\text{Na}_2\text{MoO}_4 \cdot 2\text{H}_2\text{O}$, 10 nM $\text{CuSO}_4 \cdot 5\text{H}_2\text{O}$, 296 nM thiamine HCl, 0.21 nM biotin, and 0.04 nM cyanocobalamin. Suspended in filtered synthetic seawater (described below). We purchased a K media kit from the NCMA at Bigelow Labs.

F/2 media

880 μM NaNO_3 , 36 μM $\text{NaH}_2\text{PO}_4 \cdot \text{H}_2\text{O}$, 106 μM $\text{Na}_2\text{SiO}_3 \cdot 9\text{H}_2\text{O}$, 11.7 nM $\text{Na}_2\text{EDTA} \cdot 2\text{H}_2\text{O}$, 11.7 nM $\text{Fe}(\text{NH}_4)_2(\text{SO}_4)_2 \cdot 6\text{H}_2\text{O}$, 0.9 nM $\text{MnSO}_4 \cdot \text{H}_2\text{O}$, 0.08 nM $\text{ZnSO}_4 \cdot 7\text{H}_2\text{O}$, 0.05 nM $\text{CoSO}_4 \cdot 7\text{H}_2\text{O}$, 0.04 nM $\text{CuCl}_2 \cdot 2\text{H}_2\text{O}$, 0.03 nM $\text{Na}_2\text{MoO}_4 \cdot 2\text{H}_2\text{O}$, 100 nM cyanocobalamin, 126 μM thiamine, and 100 nM biotin. Suspended in pasteurized seawater. We purchased complete liquid media from UTEX.

F/2 – Si media

882 μM NaNO_3 , 36.8 μM NaH_2PO_4 , 11.7 μM $\text{Na}_2\text{EDTA}\cdot 2\text{H}_2\text{O}$, 11.6 μM $\text{FeCl}_3\cdot 6\text{H}_2\text{O}$, 909 nM $\text{MnCl}_2\cdot 4\text{H}_2\text{O}$, 76 nM $\text{ZnSO}_4\cdot 7\text{H}_2\text{O}$, 42 nM $\text{CoCl}_2\cdot 2\text{H}_2\text{O}$, 40 nM $\text{CuSO}_4\cdot 5\text{H}_2\text{O}$, 25 nM $\text{Na}_2\text{MoO}_4\cdot 2\text{H}_2\text{O}$, 20.5 nM biotin, 4 nM cyanocobalamin, and 296 nM thiamine. We purchased liquid media from Sigma-Aldrich (G0154) at 50 \times concentration and diluted to 1 \times in filtered synthetic seawater (described below).

Synthetic seawater [RICCA Chemical Company: R8363000]

409 mM NaCl , 53 mM $\text{MgCl}_2\cdot 6\text{H}_2\text{O}$, 28 mM Na_2SO_4 , 10 mM $\text{CaCl}_2\cdot 2\text{H}_2\text{O}$, 1 mM KCl , 1 mM NaHCO_3 , 1 mM KBr , 0.4 mM $\text{SrCl}_2\cdot 6\text{H}_2\text{O}$, 1 mM H_3BO_3 , 3 mM NaOH , and 2 mM NaF . Suspended in ultrapure water.

Erdschreiber's media

2.3 mM NaNO_3 , 67 μM $\text{Na}_2\text{HPO}_4\cdot 7\text{H}_2\text{O}$, 23.7 μM $\text{Na}_2\text{EDTA}\cdot 2\text{H}_2\text{O}$, 4.3 μM $\text{FeCl}_3\cdot 6\text{H}_2\text{O}$, 2.5 μM $\text{MnCl}_2\cdot 4\text{H}_2\text{O}$, 400 nM ZnCl_2 , 100 nM $\text{CoCl}_2\cdot 6\text{H}_2\text{O}$, 200 nM $\text{Na}_2\text{MoO}_4\cdot 2\text{H}_2\text{O}$, 100 nM cyanocobalamin, and 50 μM HEPES. Suspended in pasteurized seawater. For every 1 L of media, the supplier adds 50 mL of "Soil Water: GR+ Medium" (0.05 mM CaCO_3 , 2.5% greenhouse soil, suspended in ultrapure water). We purchased complete liquid media from UTEX.

L1 media in marine broth (MB + L1)

882 μM NaNO_3 , 36.2 μM $\text{NaH}_2\text{PO}_4\cdot \text{H}_2\text{O}$, 106 μM $\text{Na}_2\text{SiO}_3\cdot 9\text{H}_2\text{O}$, 11.7 μM $\text{Na}_2\text{EDTA}\cdot 2\text{H}_2\text{O}$, 11.7 μM $\text{FeCl}_3\cdot 6\text{H}_2\text{O}$, 900 nM $\text{MnCl}_2\cdot 4\text{H}_2\text{O}$, 80 nM $\text{ZnSO}_4\cdot 7\text{H}_2\text{O}$, 50 nM $\text{CoCl}_2\cdot 6\text{H}_2\text{O}$, 10 nM $\text{CuSO}_4\cdot 5\text{H}_2\text{O}$, 8.22 nM $\text{Na}_2\text{MoO}_4\cdot 2\text{H}_2\text{O}$, 10 nM H_2SeO_3 , 10 nM Na_3VO_4 , 10 nM K_2CrO_4 , 296 nM thiamine HCl, 0.21 nM biotin, and 0.04 nM cyanocobalamin. Suspended in marine broth 2216 [5 g/L peptone, 1 g/L yeast extract, 0.41 mM $\text{C}_6\text{H}_5\text{FeO}_7$, 333.1 mM NaCl , 62 mM MgCl_2 , 26.9 mM MgSO_4 , 16.2 mM CaCl_2 , 7.4 mM KCl , 1.9 mM NaHCO_3 , 0.67 mM KBr , 0.21 mM SrCl_2 , 0.36 mM H_3BO_3 , 0.033 mM Na_2SiO_3 , 0.06 mM NaF , 0.02 mM NH_4NO_3 , and 0.056 mM Na_2HPO_4 in ultrapure water.] We purchased an L1 media kit from the NCMA at Bigelow Labs. In this instance, we suspended L1 in marine broth 2216 instead of synthetic seawater because autoclaving synthetic seawater often results in nutrients precipitating out [17] and the addition of peptone increases the media's buffer capacity, preventing excessive precipitation [18].

Spot assays (Figure 3, Figure 4, Figure 6, Figure 10)

We maintained cells on plates of TAP media with 1.5% agar under a 12/12-hr light-dark cycle at ambient temperature. One day prior to experimentation, we seeded cells in 3 mL of liquid TAP media or sterile water and grew them at ambient temperature under a 12/12-hr light-dark cycle while rotating at 46 rpm at a $\sim 120^\circ$ angle in a rotator drum. The next day, we measured the optical density at 730 nm for each strain using a SpectraMax iD3 plate reader (Molecular Devices). We diluted dense cultures to have equal concentrations of cells. We conducted a serial dilution of the samples, following a progressive pattern of (1:1, 1:2, 1:4, 1:8, 1:16), or (1:1, 1:10, 1:100, 1:1,000, 1:10,000) where noted, to gradually reduce the concentration at each successive step in either water or TAP. We spotted samples grown under each condition onto nine agar plates per growth medium in 5–10 μL volumes. We kept plates at ambient temperature overnight to allow spots to dry.

The next day, we flipped and sealed plates. We then grew three plates from each group at 17 °C or ambient temperature under a 12/12-hr light-dark cycle or at 24 °C under constant illumination. For the 17 °C condition, we grew cells in an incubator (internal dimensions 28 × 25 × 36 cm) equipped with three dimmable LED strips (48 LEDs/strip) emitting the full spectrum of visible light. Our light meter read the luminosity at 1,800 lux in this enclosed environment. We allowed cells to grow for 16–40 days, depending on the initial cell concentration, and then imaged the plates using an Azure 600 imaging system (Azure Biosystems) under “true color imaging” settings.

When comparing growth on calcofluor-white or Congo red supplemented TAP medium, we grew cells in an enclosed 32” × 32” light box equipped with three LED strips and reflective siding to ensure even, constant illumination throughout at 3–4,000 lux units. We kept the environment at ambient temperature with a beaker of water sitting inside to ensure a humid environment. We imaged the plates using the Azure 600 imaging system (Azure Biosystems) with both “true color imaging” settings and consistent Cy5 fluorescence imaging settings.

We processed all imaging data using Fiji software. Briefly, we positioned 60-pixel-in-diameter regions of interest around each colony and measured the mean fluorescence intensities of each colony from the Cy5 fluorescence images. We calculated and subtracted the mean background intensity of the media. We performed two-way ANOVA statistical analyses with Tukey’s multiple comparisons using GraphPad Prism (version 10.0.3).

Detergent treatment ([Figure 8](#))

We grew cells in liquid TAP media for 8–10 days while shaking under a 12/12-hour light-dark cycle at ambient temperature. We initially performed this experiment as a lower-throughput method with all three *Chlamydomonas sp.* strains, but adapted it using cc-124 and cc-1373 to enable high-throughput analysis. On the day of the experiment, we measured the OD₇₃₀ of each species to confirm similar cell densities. For low-throughput experiments ([Supplemental Figure 3](#)), we collected cells in 1.5 mL microfuge tubes for each reaction through centrifugation at 3,500 × g for five minutes and then resuspended the cells in 100 μL of reaction buffer (20 mM Tris-HCl; 5 mM CaCl₂; 5 mM MgCl₂). For high-throughput reactions ([Figure 8](#)), we distributed the cells between the wells of a deep 96-well, 1 mL round-bottom plate. Here, we collected cells at 2,900 × g for five minutes before resuspending in 100 μL of reaction buffer. Our attempts to do this experiment with standard flat-bottom 96-well plates were not initially successful, likely because of the reduced cell density in the small-volume wells, difficulty pelleting cells on a flat surface, and having less spatial separation between the supernatant and the pellet.

For both experimental conditions, we next added an equal volume of 0.1% Triton X-100 (bringing its final concentration to 0.05%) to treated cells or an equal volume of reaction buffer to control cells. For lower-throughput experiments, we vortexed all tubes for one minute using the Scientific Industries Disruptor Genie at 3,000 rpm. For the higher-throughput approach, we covered the plate with a sterile AeraSeal membrane (Excel Scientific Cat # BS-25) to prevent cross-well contamination and vortexed the plate for two minutes using the Scientific Industries Vortex-Genie 2 equipped with a microplate adaptor. We set the machine to vortex at 3,000 rpm, but the readout ranged between 2,000–2,800 rpm during the two-minute vortex. We immediately collected cells by centrifugation at 13,000 × g for low-throughput experiments and 2,900 × g for high-throughput experiments for five minutes. We transferred 100 μL of supernatant from each reaction across a 96-well plate and measured the OD₄₃₅ using a Molecular Devices SpectraMax ID3 plate reader (Absorption, Endpoint, Lm1: 435 nm; PathCheck: On; Detection Method: Precise; Shake Before: 00:05 [high intensity]).

Data analysis: Detergent treatment ([Figure 8](#))

We subtracted the OD₄₃₅ of reaction buffer or reaction buffer with 0.05% Triton X-100 from each measurement. We next subtracted the average OD₄₃₅ of the untreated

control cells from the corresponding values of treated cells. There was no significant difference between the untreated sample OD₄₃₅ readings. We performed statistical analyses using GraphPad Prism (version 10.0.3). Briefly, we tested for normality using a Shapiro-Wilk test, which revealed a normal distribution across treated samples. When comparing two samples, we performed an unpaired two-tailed t-test. When comparing three samples, we performed ordinary one-way ANOVA with Tukey's multiple comparisons test. The post-hoc test adjusts for multiple comparisons, controlling for type I errors (at 0.05). Asterisks in the figures indicate the adjusted p-values as follows: *p < 0.05, **p < 0.01, ***p < 0.001, ****p < 0.0001, and ns means not significant.

Magnetic fields ([Figure 11](#))

We seeded cells in 200 µL of TAP medium in black-walled 96-well plates. We grew one plate atop a 3D-printed block embedded with 24 neodymium magnets of 12 mm diameter and 3 mm height arranged in a 6 × 4 pattern. We grew the other plate atop a 3D-printed solid-plastic block to prevent excess light from entering from beneath the plate. We approximated magnetic flux density measurements for each well using a handheld digital gaussmeter. We grew cells in an enclosed environment at ambient temperature with 3,000–4,000 lux units of constant light. We measured the OD₇₃₀ using a Molecular Devices SpectraMax iD3 plate reader (Absorption, Endpoint, Lm1: 730 nm; PathCheck: On; Detection Method: Fast; Shake Before: No.). We plotted values in GraphPad Prism (version 10.0.3).

Microscopy

Sample prep: Media-dependent morphologies ([Figure 7](#), [Video 1](#), [Video 2](#))

We grew cells on 1.5% agar in the indicated media. We picked individual colonies with a sterile loop and suspended them in sterile water, placed in a 96-well plate with a #1.5 glass coverslip, and imaged immediately. For [Video 1](#) and [Video 2](#), we suspended cells in L1 media and plated on an ArrayLize glass coverslip with 400 µm flat-bottom wells. We mounted coverslips on a standard microscope slide and sealed with VALAP (1:1:1 mixture of Vaseline, lanolin, and paraffin wax).

Sample prep: Cell wall staining ([Figure 9](#))

We grew cells in liquid TAP media and collected cells through centrifugation at 2,000 rpm for one minute. We resuspended cells in TAP media with the noted concentration of calcofluor-white (CFW) stain supplemented with Evans blue (Sigma-Aldrich, SKU 18909) for 10 minutes while rotating at ambient temperature. Afterward, we washed the cells twice in fresh TAP media. For initial protocol development, we imaged the cells immediately after washes. For the datasets quantified in this pub, we fixed in freshly made 4% paraformaldehyde in PBS for 15 minutes at ambient temperature while protected from light. We then washed the fixed cells twice in PBS and stored the samples at 4 °C until imaging. Some protocols suggest adding 10% KOH while staining; however, we found this leads to a substantial increase in cytosolic staining and we don't suggest it when staining the algal cell wall.

Sample prep: Gamete enrichment for cell morphology and motility measurements ([Figure 12](#), [Video 3](#), [Figure 13](#), [Figure 14](#), [Figure 15](#))

We scooped cells from agar plates growing either *C. reinhardtii* or *C. smithii* using a sterile loop and deposited them into 100 µl of water. We scooped approximately 1 cm² from a lawn of cells. We left the cells on the benchtop overnight (16–20 hours). This incubation step promotes gamete formation. Clumps of cells and immotile cells settle to the bottom, and motile cells are enriched in the supernatant. We loaded cells from the supernatant onto agar microchambers [19] immediately before imaging. We mounted and imaged *C. smithii* and then *C. reinhardtii*. We performed the procedure four times on different days with cells obtained from the same lawn plates ([Figure 12](#)). We created the agar microchambers and loaded the cells according to a standardized protocol, aiming to load 1–3 cells per well [20].

Sample prep: Immobilizing cells for imaging organelle morphology ([Figure 16](#))

We prepared *Chlamydomonas reinhardtii* and *smithii* samples by scooping cells from a lawn plate (grown on TAP medium + 1.5% agar), inoculating 500 µl of liquid TAP medium in a 1.5 mL microcentrifuge tube, and leaving the tubes on the bench (at room

temperature) overnight in front of a grow lamp on a 12:12 light:dark cycle. The following morning, we pelleted cells (2,000 × g for 2 min), stained with PKmito ORANGE (Spirochrome) in TAP to label mitochondria (for 45 min), and then washed and resuspended in a low-gelling agarose solution (1.25% in TAP), from which we prepared a slide for imaging.

The step-by-step **protocol** we used to [immobilize cells for live imaging](#) is available on protocols.io.

Imaging: Media-dependent morphologies ([Figure 7](#), [Video 1](#), [Video 2](#))

We acquired images with a Yokogawa W1-SoRa confocal scanner unit attached to a Nikon Ti2-E inverted microscope equipped with an ORCA-Fusion BT digital sCMOS camera and a LIDA Light Engine for RGB color imaging. We used a Plan Apo λ 60× oil objective with a 1.5× magnifier or a Plan Apo λ 10× air objective. We processed all imaging data using Fiji software and the StackReg Fiji plugin from the BIG-EPFL package to correct for sample drift during extended time-lapse imaging [21].

Imaging: Cell wall staining ([Figure 9](#))

We acquired images with a Yokogawa CSU W1-SoRa confocal scanner unit attached to a Nikon Ti2-E inverted microscope equipped with an ORCA-Fusion BT digital sCMOS camera. We used a Plan Apo λ 40× objective. We acquired images at the medial focal plane of the cells in the field of view. We used standard DAPI imaging settings with the 405 nm laser set to 75% with 500 ms exposure.

Imaging: Cell morphology and motility ([Figure 12](#), [Video 3](#), [Figure 13](#), [Figure 14](#), [Figure 15](#))

We collected videos on a Nikon Ti2-E microscope equipped with a Photometrics Kinetix digital sCMOS camera. We performed differential interference contrast imaging using a Plan Apo 10× 0.45 Air objective. We collected videos with a 5.1 ms exposure with acquisition every 50 ms for three minutes. We placed a red light filter [IR

longpass, 610 nm (ThorLabs)] in the light path to maintain swimming behavior of cells [22].

Imaging: High-resolution confocal z-stacks for organelle morphology (Figure 16)

We collected images on a Nikon CSU W-1 SoRA spinning disk confocal microscope equipped with an ORCA-Fusion BT digital sCMOS camera. In order to apply deconvolution in the downstream processing, we needed to oversample in z resolution. To do this, we used a 100×/1.45 NA oil objective in 2.8× SoRa magnification mode, using ROIs of either 670 × 670 × 81 or 850 × 850 × 91. We imaged with a z-step size of 100 nm for sub-Nyquist sampling. We imaged bright-field first, then 640 nm excitation to capture chlorophyll autofluorescence, followed by 561 nm excitation for PKmito ORANGE dye, which labels mitochondria. We imaged using 561 nm excitation after 640 nm excitation because 561 nm excitation causes chlorophyll to bleach. We set exposures to 300 ms with 30% and 50% laser power for 640 and 561, respectively.

Image processing and analysis

Processing and analysis: Cell wall staining (Figure 9)

We used CellProfiler (version 4.2.5) to segment cells and measure the cell area and position. Briefly, for each image, we used the `IdentifyPrimaryObjects` command to segment objects 30–100 pixels in diameter while discarding objects that were outside of this range or objects that touched the border of the image. We then used the functions `MeasureObjectIntensity` and `MeasureObjectSizeShape` for each object. We exported the data to either a spreadsheet (when processing individual files) or to an SQLite (version 3.41.2) database (when we performed the commands in batch). We used these measurements to extract images of each cell to its own file using a custom Python (version 3.10.12) [script](#). We next ran these extracted image files through CellProfiler again to generate new cell position coordinates. We performed the subsequent analysis using Python. We used these measurements to align each cell so the major and minor axis intersect at the centroid of the image. We then padded every image with empty pixels to ensure the file dimensions were identical across samples.

For each cell, we then measured the intensity profile through the major and minor axes using a five-pixel-diameter linescan and extracted individual peak intensities and the distance between the half-maximum of each peak. We further analyzed these extracted values in GraphPad Prism (version 10.0.3). Raw data used in this analysis is accessible on [Zenodo](#). We used ChatGPT to generate the Python code for this processing and analysis.

Our **calcofluor-white-stained microscopy data** are available on [Zenodo](#).

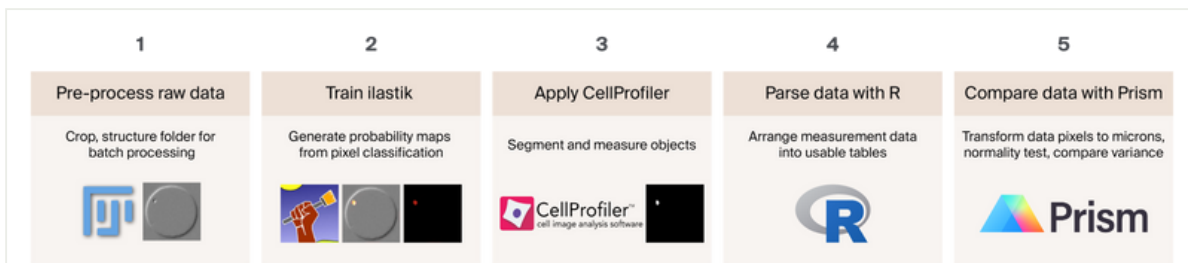


Figure 1

Visual overview of our image processing and analysis workflow.

We performed regression analyses and generated violin plots in R and used Prism for scatter plots.

Processing: Cell morphology and motility

Pre-processing: Cell morphology

We segmented images of individual microchambers using an interactive Fiji macro [23] (Figure 1). We applied the pixel classifier to the first 100 frames (five seconds of video) of each three-minute video to generate probability maps. We determined which frames were in focus by first applying a Laplacian filter to each frame then calculating the variance of those values within each frame. This metric, the “variance of the Laplacian,” has been shown to provide a good estimate of image focus. For a time series, peaks in the variance of the Laplacian across time indicate frames that are in the sharpest focus [24]. As expected, when we plotted these variance values from the first frame to the last (frame 3600), we saw peaks and valleys. We selected the frame

corresponding to each peak (the local maximum) and then took the three frames before and after that frame for further analysis. These data are available on [Zenodo](#).

Our **focus-filtered time-lapse data and measurements** are available on [Zenodo](#) (DOI: [10.5281/zenodo.8326749](https://doi.org/10.5281/zenodo.8326749)).

Training: Cell morphology

We trained a pixel classifier to distinguish cells from background using ilastik [25] ([Figure 1](#)). We performed training on a subset of images of 3,600 frames of the three-minute videos. The training subset consisted of every 60th frame in the videos, approximately 2% of the total frames. We used the automatically suggested features in ilastik for the pixel classification. We also tested applying the pixel classifier to a subset of images of cells in focus. We performed training on all of the microchambers to ensure that we captured the full diversity of images in our experimental replicates. The training set and the classifier are available on [Zenodo](#).

Segmentation, measurement, and data parsing: Cell morphology

We segmented objects (i.e. cells) using a probability cutoff of 50% for pixel values, with a size range between 5–40 pixels in CellProfiler [26] in our initial studies. We chose this pixel probability cutoff based on a qualitative visual inspection of the segmentation. We determined the size cutoff by measuring cells in CellProfiler and adding a 10-pixel buffer on both ends of the size range. We then collected measurements of the objects using CellProfiler.

To increase the rate of image processing in preparation for future high-throughput work, we wrote Python scripts to segment cells and measure objects in the images. This decreased processing time from hours to seconds. We collected specific cell morphology and motility measurements, including cell area, major axis length, minor axis length, and frame-to-frame linear and angular displacement. You can find a detailed protocol, along with code, in the [GitHub repository](#) associated with this pub. We used ChatGPT to write rough drafts of scripts, to comment code, and for troubleshooting code performance.

Our **Fiji macro**, **CellProfiler pipeline**, and **code** in R and Python are available in this [GitHub repository](#).

Graphical analyses: Gross cell morphology and motility

([Figure 12](#))

To assess empirical measures, we used GraphPad Prism and transformed the data from pixels to microns, tested for outliers to clean the data [ROUT (Q = 1%)], and then tested for normality (D'Agostino & Pearson test, Anderson-Darling test, Shapiro-Wilk test, and Kolmogorov-Smirnov test). If data were distributed normally, we partitioned the variance by doing a one-way ANOVA and Tukey's multiple comparison test to determine the treatments that differed from one another. If the data were not normal, we performed the non-parametric equivalent, a Kruskal-Wallis test and Dunn's multiple comparisons test. In both cases, the post-hoc tests adjust for multiple comparisons, controlling for type I errors (at 0.05).

Given potential experiment-level variability, we then used R to perform a linear regression to remove the effect of the experiment on area and analyzed the residuals. We compared the residuals using a Kruskal-Wallis test followed by a Bonferroni correction ([Supplemental Figure 4](#)). We used this same approach to analyze the velocity and angular velocity, which you can see in the accompanying notebook ([motility_v3_pub.ipynb](#)) in the R script folder of our [GitHub repo](#) ([Figure 14](#), B and C; [Figure 15](#), A and B). We used ChatGPT to help with scripting and commenting this code.

Graphical analyses: Cell motility behavior ([Figure 14](#), [Figure 15](#))

We smoothed velocity parameters (forward and angular velocity, R function `ksmooth` (bandwidth = 10)) prior to calculating the autocorrelation and joint distribution between forward and angular velocity. This smoothing procedure helped reduce noise in the velocity measurements that may arise from segmentation and tracking. We calculated autocorrelations of forward and angular velocity over a five-second window using the R function `acf`. We inferred the joint distributions between forward and angular velocity by a probability density function (PDF) calculated using the function `kde2d` in the R package MASS (Venables & Ripley 2002) using a bandwidth of 100. We calculated differences between joint distributions by first normalizing each PDF by its maximum

value (resulting in comparable scales between 0 and 1) and then subtracting one from the other. See the accompanying motility notebooks in the R folder of our [GitHub repo](#).

Visual analyses: Cell morphology and motility

To visualize the average differences in cell morphology between the two species, we calculated a cell of average size and shape based on our empirical mean and standard deviation measurements using a custom Python script created with ChatGPT ([Figure 11, D](#)). We also used ChatGPT to comment this code.

To improve our visual assessment of the morphological differences between species, we then averaged and superimposed images of individual cells ([Video 3](#)). First, we masked individual cells with image objects. We reoriented the cells to swim "up" in the image based on the first few frames, and we aligned the major axis of the cell with the y-axis. To visually assess differences in motility between species, we binned tracks by the average absolute frame-to-frame angular displacement of each track. For each bin, we superimposed the tracks of each species ([Figure 13](#)). A detailed protocol is available in the [GitHub repository](#) associated with this pub. We used ChatGPT to write rough drafts of scripts, comment code, and troubleshoot code performance.

Processing and analysis: Visualizing organelle morphology

To achieve the subcellular resolution necessary to obtain morphology measurements of organelles, we developed a workflow (using open-source tools) to go from the raw image data to volumetric measurements of the chloroplasts and mitochondria ([Figure 2](#)). We wrote macros to batch-process the images using two plugins in Fiji (with the help of ChatGPT). One was the "[PSF Generator](#)" plugin, which we used to generate a theoretical point spread function (PSF) for each wavelength given the resolution of our images. The PSF images we used for 561 nm and 640 nm for each resolution are available along with the raw data on [Zenodo](#). The other plugin we used was [DeconvolutionLab2 \[27\]](#), where we first performed a background subtraction (rolling ball = 300) and then applied the regular inverse filter (RIF) algorithm to each channel.

Our **high-resolution confocal z-stacks** for visualizing organelle morphology are available on [Zenodo](#) (DOI: [10.5281/zenodo.10127603](https://doi.org/10.5281/zenodo.10127603)).

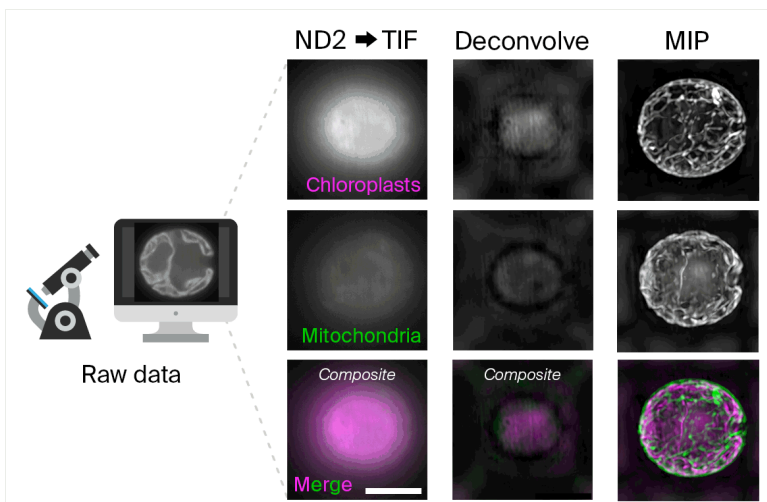


Figure 2

Overview of the image processing workflow to generate volumetric organelle data from *Chlamydomonas* parent species following high-resolution microscopy.

The first step converts the data from the Nikon ND2 files to TIF and splits the channels, one for 640 excitation showing the chloroplasts, and one for 561 excitation showing the mitochondria. Next, we deconvolve these TIF files using the DeconLab2 Fiji macro along with the point spread function (PSF) files. Finally, we generate maximum intensity projections (MIPs) as the deconvolved channels are recombined into a composite image.

Writing and coding

We used ChatGPT to suggest wording ideas and streamline/clarify content, and then edited the AI-generated text. We also used ChatGPT to help write, clean up, and comment our code.

The results

Growth on various media

We decided to grow both *Chlamydomonas* species on a variety of media to identify environmentally driven species-species differences in growth. In this initial study, we included two *C. reinhardtii* strains of opposite mating types to ensure any observed phenotypic differences aren't mating-type dependent or strain-specific.

We can maintain both *C. reinhardtii* and *C. smithii* in standard TAP (tris-acetate-phosphate) media [13]. We were surprised to see *C. smithii* outgrowing *C. reinhardtii* on other Chlorophyceae (green algae) media – soil extract media and Bristol media (Figure 3). Bristol media is richer than TAP media in several components, including nitrogen, phosphate, and multiple salt ions, including Mg^{2+} , Na^+ , and K^+ , but lacks the trace heavy metals found in TAP media. Soil extract media is Bristol media supplemented with 4% pasteurized soil, which likely contains trace metals similar to TAP media.

The few *C. reinhardtii* colonies we did see looked qualitatively more yellow compared to the usual green, a sign of chlorosis, which is consistent with poor nutrition [28], suggesting *C. smithii* is more adaptable to high-nutrient media than *C. reinhardtii*.

The temperature and illumination conditions we tested (Supplemental Figure 1, Supplemental Figure 2) had no obvious impact on colony growth, except visible colonies started to appear quicker under constant illumination in a controlled 24 °C environment, consistent with previous work [29]. We therefore decided to test just those growth conditions going forward.

Both species displayed slow growth on potassium nitrate-based Kuhl's media, though *C. smithii* grew slightly better. Surprisingly, we observed *C. smithii* growing on plates consisting of 1.5% agar in only ultrapure Milli-Q filtered water, even though we washed cells three times in ultrapure water prior to plating to prevent any media transfer (Figure 3).

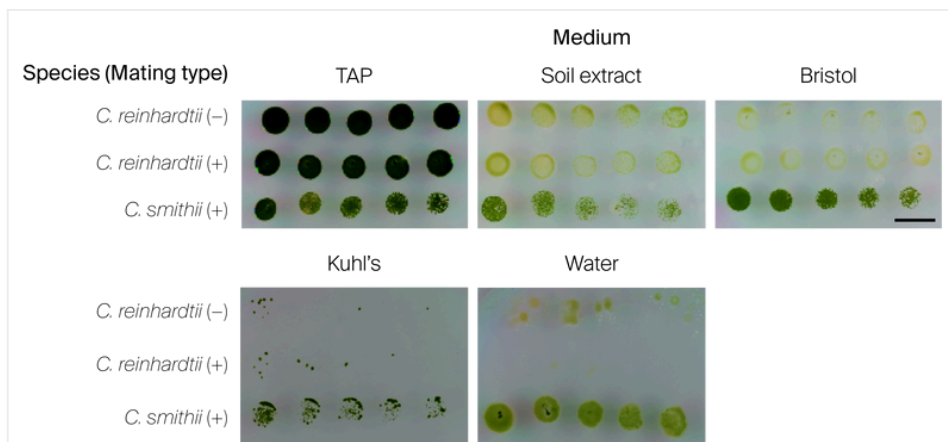


Figure 3

Both species grow on TAP media, but *Chlamydomonas smithii* can also grow on soil extract media, Bristol media, Kuhl's media, and water.

Representative spot assays of *C. reinhardtii* (cc-124 and cc-125) and *C. smithii* (cc-1373) on TAP (tris-acetate-phosphate) media, soil extract media, Bristol media, Kuhl's media, or ultrapure water at 24° C under constant illumination for 16 (top row) to 40 days (bottom row) based on the initial cell density. Serial dilutions run 1:1, 1:2, 1:4, 1:8, 1:16. Scale bar: 10 mm.

For additional temperature and light conditions, see [Supplemental Figure 1](#).

Since *C. smithii* was able to grow on rich media that includes ~0.4 mM sodium chloride, we wondered if *C. smithii* could grow on high-salt marine media. We spotted the three *Chlamydomonas* cultures onto different solid marine media that are often used to grow diatoms and other marine protists, which we already had in-house [30] [31][32].

We did not observe any growth on K media, F/2 media, F/2 lacking silica, or synthetic seawater on its own (Figure 4). However, to our surprise, we observed slow, limited growth of *C. smithii* on Erdschreiber's media and on marine broth supplemented with L1 nutrients (MB + L1) (Figure 4), which contain 409 mM NaCl and 333 mM NaCl, respectively. K media and L1 media are very similar except for the tris and ammonium chloride in K media. Since K media was suspended in synthetic seawater and L1 media

was suspended in marine broth, we suspected that the peptone, yeast extract, and ferric acid found in marine broth might be responsible for the growth of *C. smithii* on MB + L1 plates, consistent with reports that *C. smithii* shows more heterotrophic growth than *C. reinhardtii* strains [7]. Evolutionary studies show some *C. reinhardtii* strains are able to adapt to high-salt conditions and wild marine *Chlamydomonas* species have been isolated [33][34], so it follows that *C. smithii* could survive on marine media, but it's still an intriguing trait that distinguishes the species from our *C. reinhardtii* strains.

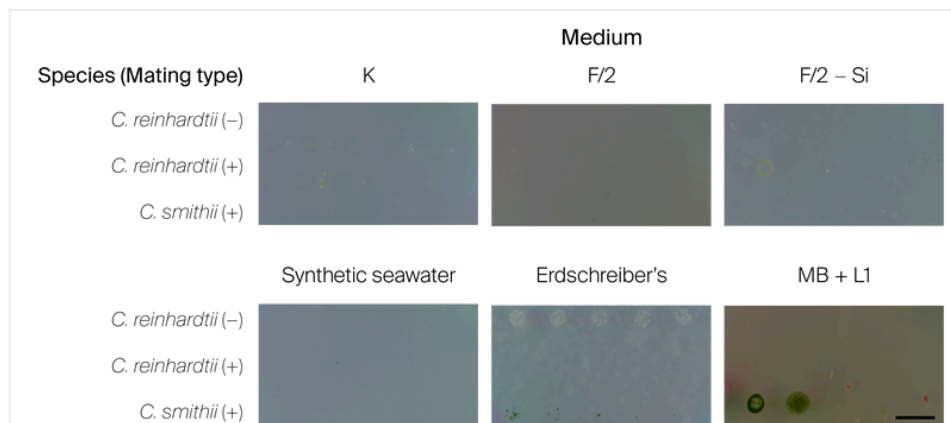


Figure 4

***C. smithii* can grow slowly on high-salt Erdschreiber's media and marine broth with L1 nutrients included.**

Representative spot assays of *C. reinhardtii* (cc-124 and cc-125) and *C. smithii* (cc-1373) on K media, F/2 media, F/2 media lacking silica, synthetic seawater, Erdschreiber's media, or marine broth (MB) with L1 nutrients, all grown at 24° C under constant illumination for 16–40 days based on initial cell density. Serial dilutions run 1:1, 1:2, 1:4, 1:8, 1:16. Scale bar: 10 mm.

For additional temperature and light conditions, see [Supplemental Figure 2](#).












Species Media	<i>C. reinhardtii</i>	<i>C. smithii</i>
TAP		
Soil extract		
Bristol		
Marine broth +L1 nutrients		
Erdschreiber's		
Kuhl's		
Ultrapure water		

Figure 5

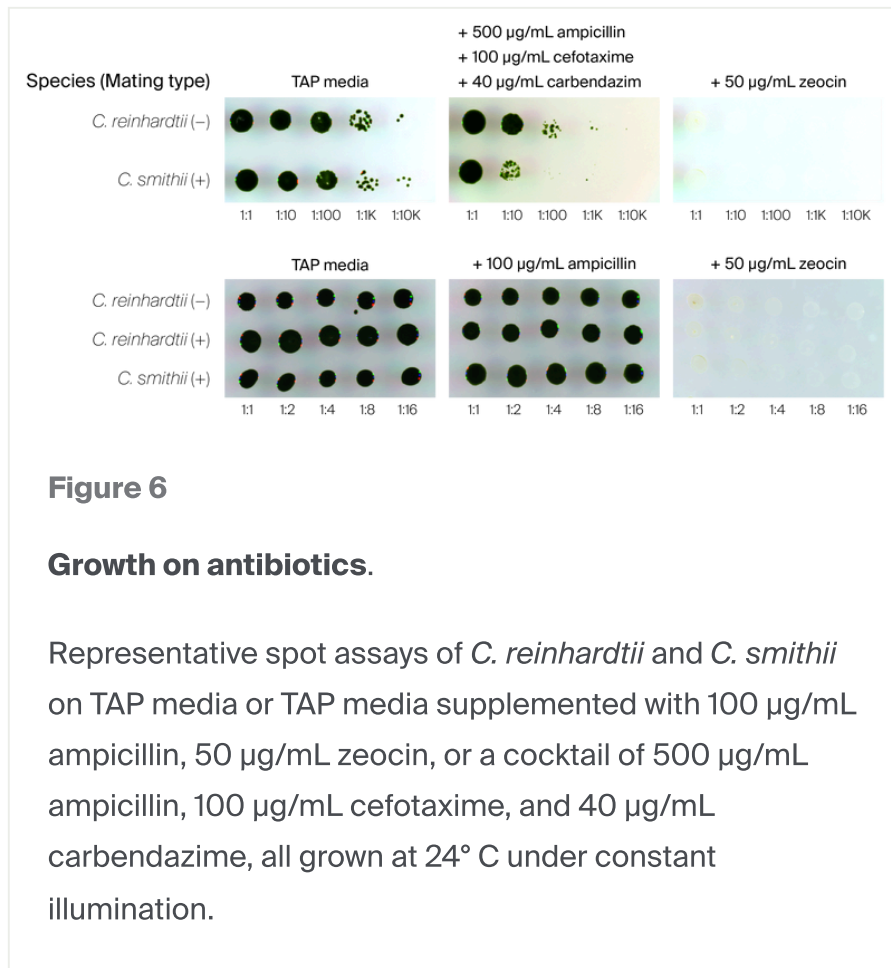
Visual summary of growth patterns on different types of media.

The number of *Chlamydomonas* icons indicates qualitative growth rates: 3: fast, 2: medium, 1: slow, 0: none. The color of the cell icon indicates the color of the colonies. The *C. reinhardtii* column represents both strains cc-124 and cc-125.

We did not observe growth on F/2, F/2–Si, K, or synthetic seawater.

We next tested each species' sensitivity and resistance to antibiotics by growing all strains on TAP media supplemented with 100 µg/mL ampicillin or 50 µg/mL zeocin (**Figure 6**). As expected, we observed that both species were sensitive to zeocin, a broad-spectrum antibiotic known to prevent cell division in *C. reinhardtii* [35], and resistant to ampicillin, an antibiotic used primarily to reduce bacterial growth. Further,

we found that both species can survive on TAP media supplemented with a harsh antibiotic/fungicide cocktail consisting of 500 $\mu\text{g}/\text{mL}$ ampicillin, 100 $\mu\text{g}/\text{mL}$ cefotaxime, and 40 $\mu\text{g}/\text{mL}$ carbendazim [36], but *C. smithii* appeared to be more sensitive to this cocktail.



Morphological differences after growing on different media

We next took a closer look at single-cell morphology after growth on different types of media. Interestingly, there were no obvious morphological differences between cells grown on freshwater media or Erdschreiber's media. However, cells grown on MB + L1 were larger and either amorphous when suspended in media ([Video 1](#) and [Video 2](#)) or swollen when suspended in water ([Figure 7](#)).



Figure 7

***C. smithii* cells become large and round on MB + L1 media.**

Representative color images of *C. smithii* grown on the noted media and then resuspended in water for imaging. TAP: tris-acetate-phosphate; MB + L1: marine broth with L1 nutrients added.

When grown on MB + L1 media, we noticed several large *C. smithii* cells with oblong morphologies that quickly rounded up after intense light exposure on the microscope ([Video 1](#)). These cells retained their green pigmentation and internal dynamics throughout the experiment, suggesting the cells were alive ([Video 2](#)). Surprisingly, we were unable to observe cell division occurring over a 67-hour period. We streaked these cells back onto TAP media and they returned to their normal morphology, confirming that this observation was a result of growth on MB + L1 and not contamination. Because we observed this phenotype in cells grown on MB + L1, but not Erdschreiber's media, we assume the phenotype is not solely salt-induced, but, rather, dependent on the presence of peptone, yeast extract, or ferric acid. Similarly, when grown in media supplemented with peptone, the gram-negative bacteria *Azotobacter vinelandii* reportedly takes on a “fungoid” morphology [37], reminiscent of these amorphous *C. smithii* cells, suggesting supplemental peptone could be responsible for this phenotype. *C. reinhardtii* did not grow on any marine media so we did not observe this morphology in either *C. reinhardtii* strain, however, it will be

interesting to see if *C. reinhardtii* grown in TAP media supplemented with peptone become similarly amorphous!

0:00 / 0:02



Video 1

***C. smithii* cells becoming more round upon intense light exposure.**

We grew *Chlamydomonas smithii* cells on 1.5% agar plates supplemented with L1 nutrients and marine broth. We imaged isolates in 400 μm glass wells in L1 media (lacking silica) at 30 minutes/frame.

0:00 / 0:03

Video 2

Amorphous *C. smithii* cells retain healthy color before and after morphological changes.

We grew *Chlamydomonas smithii* cells on 1.5% agar plates supplemented with L1 nutrients and marine broth. We imaged isolates in 400 μm glass wells in L1 media (lacking silica) at 30 minutes/frame. We captured initial and final frames in RGB, while the intermediate frames were in grayscale.

Sensitivity to detergent and cell wall structure

We next compared sensitivity to detergent by treating each strain with 0.05% Triton X-100 to disrupt the cell membrane and release chlorophyll from the cell body. The cell wall can protect the cell membrane from this detergent, preventing lysis from occurring [38]. We collected the lysed cells through centrifugation and quantified the chlorophyll fluorescence in the supernatant as a proxy for total lysis. We observed visible lysis after either one-minute or two-minute treatments with 0.05% Triton X-100 based on visible green pigment in the supernatant. The amount of chlorophyll released was consistently greater in *C. smithii* cultures compared to *C. reinhardtii* cultures (Figure 8, Supplemental Figure 3), suggesting that *C. smithii* is more sensitive to lysis by detergent.

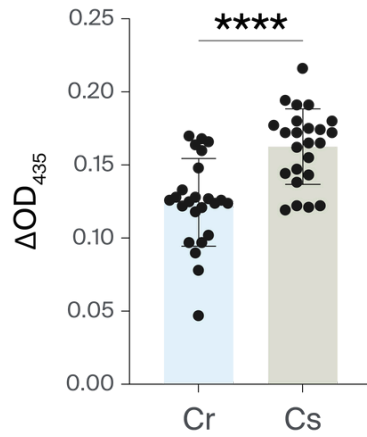


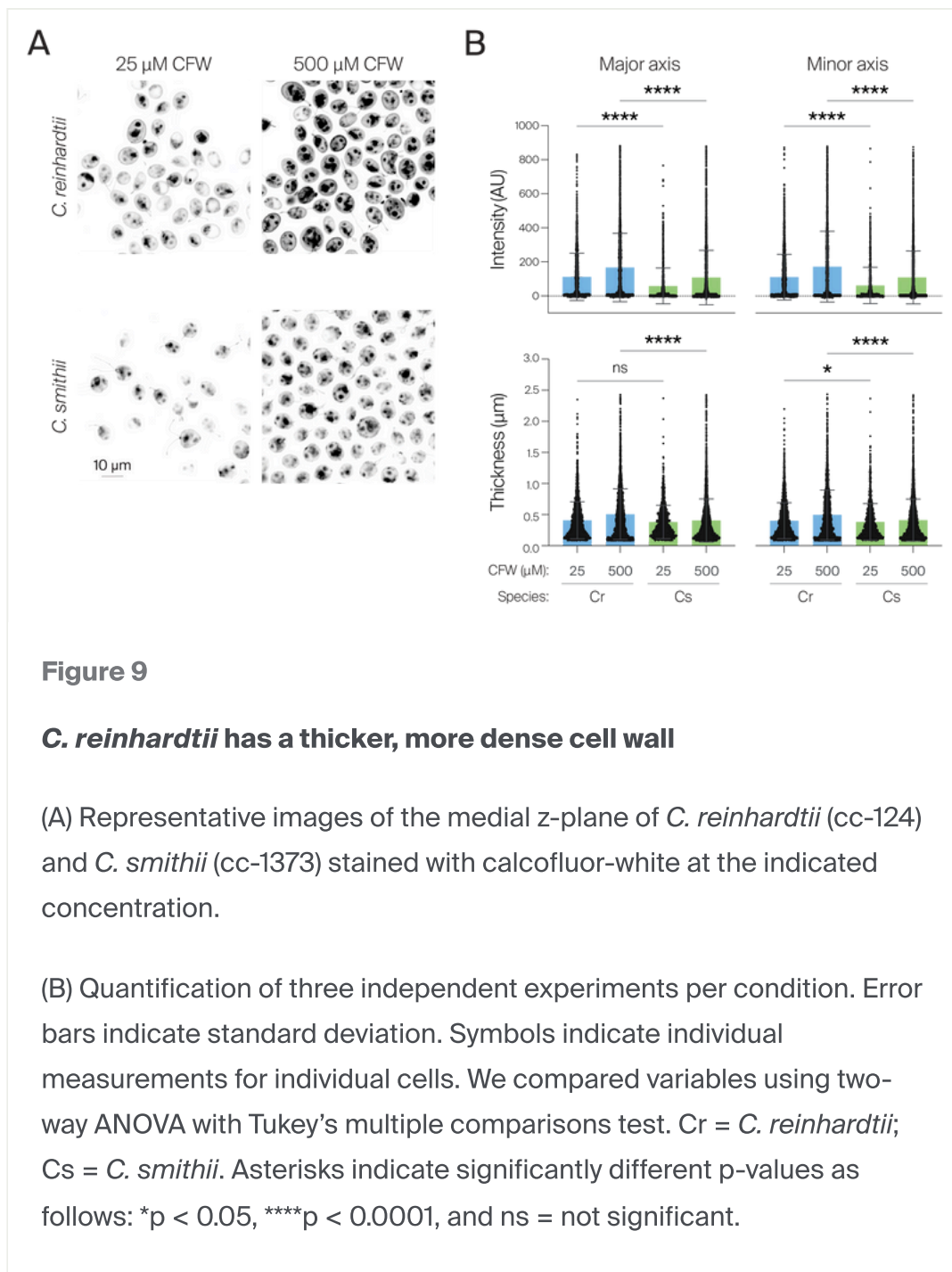
Figure 8

***C. smithii* is more prone to detergent-induced lysis.**

Bar graph representing the mean chlorophyll content found in the supernatant of lysed cells after 2 min treatment in 0.05% Triton X-100.

Individual values represent the 24 individual treatments after subtracting the mean of 12 individual untreated controls. Cr = *C. reinhardtii*; Cs = *C. smithii*. Error bars depict standard deviation. We compared treatments using an independent t-test ($t = 4.716$, $df = 46$, $p < 0.0001$). Asterisks indicate a significantly different p-value: **** $p < 0.0001$.

Since *C. reinhardtii* is more resistant to detergent-induced lysis, we were curious if the *C. smithii* cell wall is less protective than the *C. reinhardtii* cell wall. We stained both species with calcofluor-white (CFW), a fluorescent dye that binds to the cellulose and chitin in the algal cell wall [39]. We incubated *C. reinhardtii* and *C. smithii* with either 25 μM or 500 μM CFW for 10 minutes, fixed the cells in formaldehyde, and imaged them by spinning disk confocal microscopy. While 25 μM CFW was sufficient to visualize the *C. reinhardtii* cell wall, we didn't observe noticeable *C. smithii* staining until we treated the cells with 500 μM CFW (Figure 9, A), suggesting that *C. smithii* may have a cell wall that is either thinner or of a different composition than *C. reinhardtii*.



We performed batch image processing and analysis on these cells to measure the fluorescence intensity and thickness of the CFW stain by measuring the intensity profile through the major and minor axes of each cell. We extracted the exterior peak values to distinguish between cell wall staining and internal dye uptake or non-specific fluorescent signal. Consistent with our observations that *C. reinhardtii* cells are more resistant to detergent-induced lysis ([Figure 8](#)), our analysis indicates the fluorescent stain intensity and thickness of the *C. reinhardtii* cell wall is greater than that of *C.*

smithii (Figure 9, B), suggesting a more protective cell wall. These differences were more apparent between species when stained with 500 μ M CFW.

We're excited to be able to visualize these cell wall differences through fluorescence microscopy, but eager to adapt these methods to a more high-throughput approach. Studies using yeast have identified cell wall variants within populations by growing colonies on solid media supplemented with different concentrations of CFW or the red textile dye Congo red, both of which have been shown to disrupt cell growth through their interactions with the cell wall [40][41]. Similarly, others have found that Congo red limits the growth of microalgal species *Chlorella vulgaris* [42] and *Pseudokirchneriella subcapitata* [43], making this a promising approach to probe for cell wall integrity and function in high throughput.

To test this, we supplemented 1.5% agar TAP media plates with 250 μ M Congo red or 50–500 μ M CFW and performed logarithmic serial dilution spot assays with the two parental species and a *C. reinhardtii* cw2 cell wall mutant [15] (cc-1731) as a control (the studies described above suggest CFW and Congo red inhibit growth of cell wall mutants) (Figure 10, A). We imaged the plates using standard Cy5 filter settings to measure chlorophyll fluorescence as a readout of cell density.

Interestingly, there were no substantial growth defects in any of the strains when grown on 50–500 μ M CFW, suggesting that CFW isn't inhibiting cell growth. However, there was abundant precipitation in the media, so it's possible the CFW was inactive. We did observe a significant decrease in colony growth when we plated cells on TAP media + 250 μ M Congo red. We observed a drastic increase in Cy5 fluorescence in colonies grown on Congo red-supplemented media, even though the colonies appeared to be similarly dense and the media itself did not appear to have fluorescent properties. Recent reports indicate that Congo red's fluorescent properties are enhanced when bound to polysaccharides [44], which could explain the increased fluorescence intensity since the *Chlamydomonas* cell wall is polysaccharide-rich. To make relative comparisons, we normalized the growth of all media types to growth on standard TAP media.

In our analysis (Figure 10, B), we were unable to distinguish between wild-type *C. reinhardtii* and *C. smithii* cells grown on media containing Congo red, but there was significantly less growth of the *C. reinhardtii* cell wall mutant. This suggests that the assay is sufficient to identify *Chlamydomonas* cell wall mutants, but not sensitive enough to identify the subtle differences in the *C. reinhardtii* and *C. smithii* cell walls.

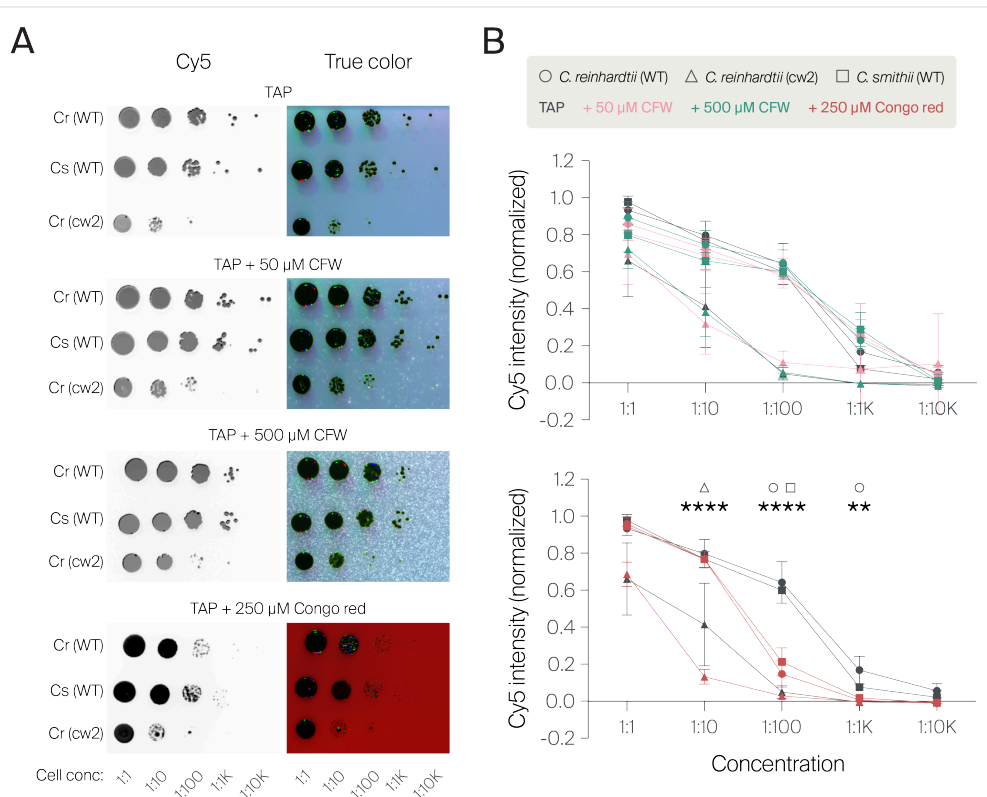


Figure 10

Congo red, but not calcofluor-white, inhibits growth of a cell wall mutant.

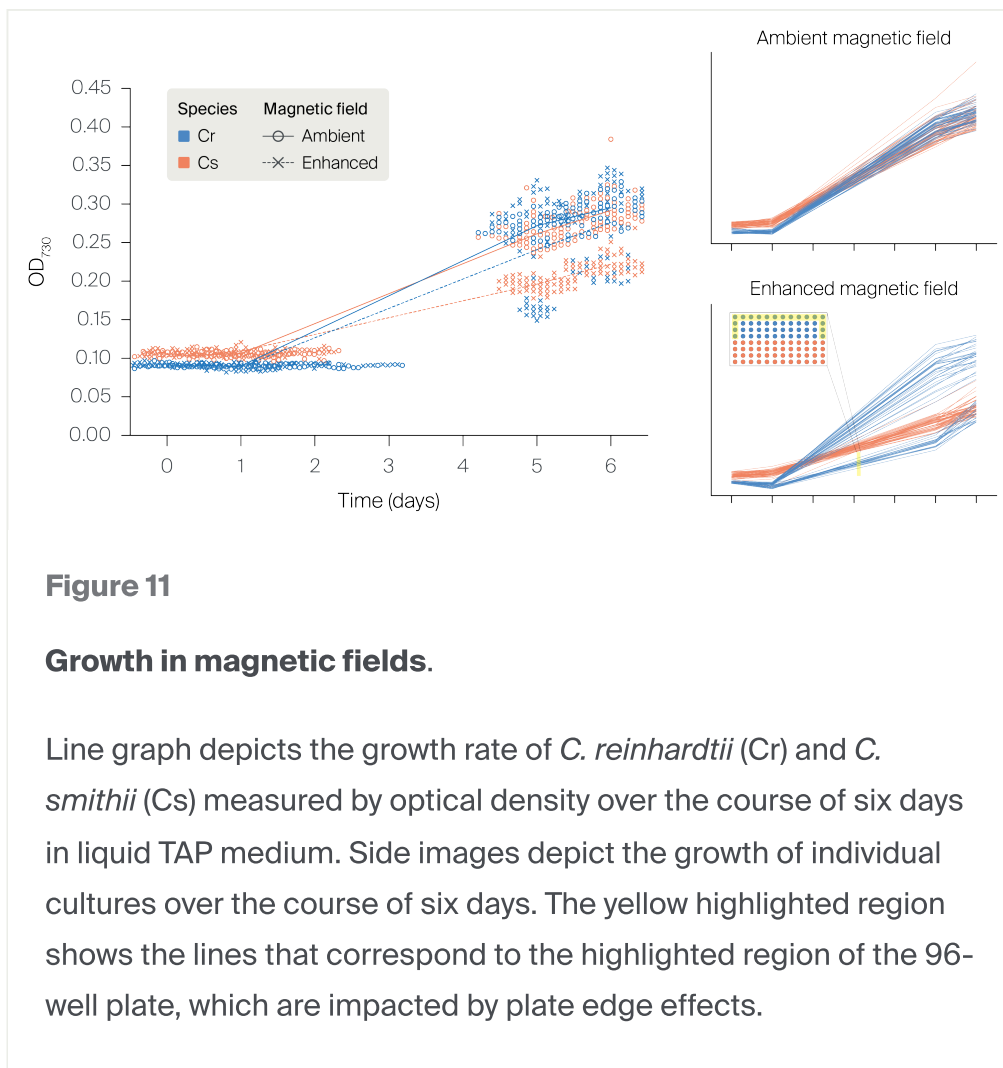
(A) Representative images of *C. reinhardtii* (WT), *C. smithii* (WT), and *C. reinhardtii* (cw2) growth on 1.5% agar TAP media or 1.5% agar TAP media supplemented with 50 μ M calcofluor-white, 500 μ M calcofluor-white, or 250 μ M Congo red. We seeded each plate from the same cultures and grew it in the same environment. Left column: Fluorescent signal excited by Cy5 settings. Right column: True-color images.

(B) Quantification of colony growth. Analysis included six sets of spot assays per supplemented medium and two control sets of spot assays on standard TAP medium. Error bars indicate the standard deviation. We omitted error bars when the deviation was less than the size of the symbol on the graph. We compared species growth between conditions using two-way ANOVA with Tukey's multiple comparisons test. Significance is depicted in the figure as: ** $p < 0.01$, **** $p < 0.0001$.

Recent work showed that a *C. reinhardtii* strain without a cell wall grows slower when exposed to a magnetic field [45]. We were curious to see if we could use this assay to distinguish between the two parent species, hypothesizing that *C. smithii*'s thinner cell wall (Figure 9) might make it more sensitive to magnetic fields.

We seeded two 96-well plates with *C. reinhardtii* and *C. smithii* cultures at equal concentrations and measured the optical density at 730 nm (OD₇₃₀) multiple times over the course of six days. We grew the cells in the same enclosed environment but grew one atop a block of plastic embedded with 24 evenly arranged neodymium magnets and the other atop a block of solid plastic. The magnetic flux density of the blocks ranged from 10–60 millitesla across the magnetic block and 0.00–0.05 millitesla across the plastic block.

Surprisingly, we observed reduced growth of both species when grown on the magnetic block, but *C. smithii* was more strongly inhibited (Figure 11)! When we plotted the growth of each colony, instead of just the mean, we noticed two populations of *C. reinhardtii* cells grown in the enhanced magnetic field. Upon further inspection, all of the cultures that were in the lower growth population were in the edge wells of the 96-well plate. Curiously, we did not observe any measurable plate effects in *C. smithii* on either plate or for *C. reinhardtii* in the ambient magnetic field. However, this intriguing assay appears to be sensitive enough to distinguish between the two species and we will continue to optimize it for high-throughput experiments.



Gross differences in cell morphology and motility

To compare the morphology and swimming behavior of the two species, we designed an experiment to collect two-dimensional measurements of motile gametes of both *C. reinhardtii* and *C. smithii*.

First, we loaded a gamete-enriched population of motile cells into agar microchambers [19][20]. We selected approximately thirty 100 μm -diameter microchambers for imaging each algal species. Each microchamber contained 1–3 cells. We collected three-minute videos of microchambers at 20 frames per second for subsequent cell morphology analysis. We performed four replicates of the experiment, conducted on different days but with cells obtained from the same lawn plate. We used bright-field illumination for Experiment 1 and differential interference

contrast for Experiments 2–4. Following image acquisition, we used the ilastik software package to classify pixels as containing information from a cell or containing information from the background [25]. This classification creates probability maps that we then used in CellProfiler [26] to segment cells and generate a dataset of 2D morphological measurements (see [Figure 1](#) for an overview of our workflow). We also analyzed motility patterns from these datasets, which we discuss below (read on about morphology or [click to skip straight to motility](#)).

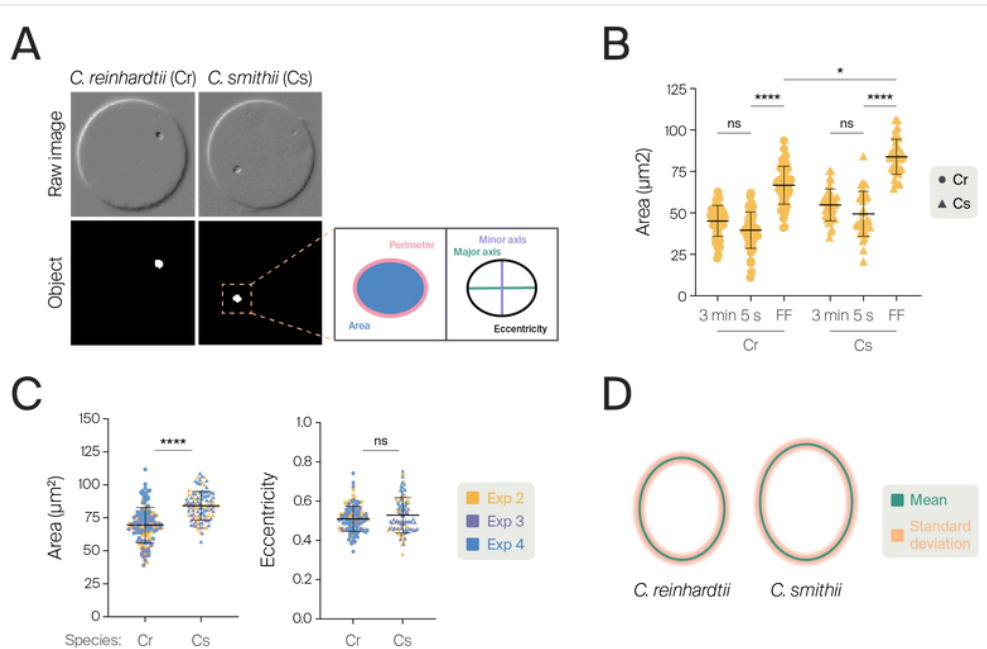


Figure 12

2D morphological measurements for each species determined from video data of swimming cells.

(A) Two single frames showing motile *C. reinhardtii* and *C. smithii* cells, each within a 100 μm -diameter agar microchamber. We've diagrammed the morphology measurements that we collected.

(B) Comparison of area measurements for experiment 2 (Exp 2) between the full dataset (3 min), a random subset of data (first 5 s), and the focus-filtered (FF) data.

(B–C) Each point in the scatter plot is the mean of measurements from the frames with an object in focus in the video of a single microchamber. We are showing the filtered dataset for experiments 2–4, as we collected these using differential interference contrast. We compared treatments using a one-way ANOVA ($F(3,129) = 8.229$, $p < 0.0001$) and Dunn's multiple comparisons test. Cr = *C. reinhardtii*; Cs = *C. smithii*. Asterisks indicate significantly different p-values as follows: * $p < 0.05$, ** $p < 0.01$, **** $p < 0.0001$, and ns = not significant.

(C, left) *C. smithii* has a larger area footprint than *C. reinhardtii* by $\sim 14 \mu\text{m}^2$ for each experiment as determined by a Mann-Whitney

test, $U = 3241$, $p < 0.0001$.

(C, right) The cell shape (eccentricity) is not statistically different between species as determined by a Mann-Whitney test, $U = 7560$, $p = \text{ns}$. However, when we performed a linear regression and controlled for batch effects, there was a statistical difference in eccentricity (see [Supplemental Figure 4](#) for complete dataset and linear regression analysis). Horizontal lines indicate the mean, error bars show the standard deviation.

(D) Drawings represent the average measurements for gametes of each species. Green lines indicate the mean and the orange glow indicates the standard deviation. See Video 3 for a qualitative assessment of the raw data.

Cell morphological data

For each segmented cell, we measured the area, perimeter, major axis, minor axis, and eccentricity ("roundness") ([Figure 12](#), A). We first decided to assess how many frames were necessary to quantify these different morphology measurements. For one replicate (Exp 2), we analyzed all 3,600 frames of the three-minute videos, but the computational processing time for the analysis was long (many days). Next, we compared area measurements from the full three-minute videos (3,600 frames) with area measurements from just the first five seconds of video (100 frames) ([Figure 12](#), B, [Supplemental Table 1](#)). Although this method let us compare five morphology measures between the two species, the first 100 frames were a random subset of the data and included many frames with the cells out of focus. We therefore decided to use a pre-processing step to identify frames where cells were in focus, thus providing the optimal frames to estimate morphological characteristics of the cell.

To do this, we used a metric called "variance of the Laplacian," a measure commonly used to identify frames that are in focus in a series of images [\[24\]](#). The first step in calculating this metric is to convolve the images with a Laplacian matrix. We found that this transformation resulted in qualitatively different outputs when applied to bright-field images (Exp 1) as compared to differential interference contrast images (Exp 2–4) [\[46\]](#). For this reason, we excluded Exp 1 from our morphology data processing and results. Not only did this subsampling approach improve our processing time, but it

also led to higher values for morphology measurements (e.g., area) by eliminating frames where the object was out of focus and values only captured part of the object ([Figure 12, B](#); [Figure 12, C](#)). We proceeded to analyze the focus-filtered datasets for all measures of morphology.

xlsx Supplemental Table 1 - Morphology stats.xlsx

Download

Despite the fact that these were clonal populations, they displayed a surprising amount of variation for each measure ([Figure 12, C](#)). To control for the possibility that factors specific to each experimental replicate might be contributing to this variation, we performed a regression analysis controlling for experimental trial and plotted the residual variation attributable to species identity. This showed that species identity was the most reliable and strongest factor determining differences for all measures ([Supplemental Figure 4, B](#)), though we did observe significant variation between experiments. Both measurements of area and perimeter differed between species across all four experiments, with *C. smithii* being larger. The mean area of *C. smithii* is 69.53 ± 13.44 (standard deviation) μm^2 , whereas the mean area of *C. reinhardtii* is 84.16 ± 10.85 (SD) μm^2 ([Figure 12, C and D](#)). The perimeter, as well as the major and minor axes, were all longer in *C. smithii* compared to *C. reinhardtii* ([Supplemental Figure 4](#)). However, the eccentricity was similar for both species [*C. reinhardtii* is 0.51 ± 0.06 (SD) compared to 0.53 ± 0.09 (SD) for *C. smithii*] ([Figure 12, C](#)), but this difference was statistically significant when we performed a linear regression to remove experimental batch effects ([Supplemental Figure 4](#)).

0:00 / 0:09

Video 3

Diversity and mean of 2D morphology measurements of the two species.

We segmented cells in images and computationally aligned them so that the swimming direction is “up” and the major axis of the cell is coincident with the Y-axis. We’re displaying a random subset of cells from three experiments.

Cr = *C. reinhardtii*. Cs = *C. smithii*. The “Merge” panel on the right shows cumulative average projections of all the cells, with Cr in cyan and Cs in magenta.

In summary, we found that, in these two-dimensional projections, the gamete form of *C. smithii* is about $14 \mu\text{m}^2$ (21%) larger than its *C. reinhardtii* counterpart and is slightly more oblong at this life-history stage.

Differences in cell swimming behavior: Single-cell swimming

We then analyzed the same datasets of swimming cells to understand whether the gametes of these two species differ in motility behaviors. We noticed clear, qualitative differences in the motility of these two *Chlamydomonas* species ([Figure 13](#)). In circular agar microchambers, *C. reinhardtii* tends to occupy the periphery, while *C. smithii*

explores more uniformly. *C. reinhardtii* appears to perform longer trajectories while exploring, while *C. smithii* demonstrates more frequent turns and short trajectories ([Figure 13](#)). Specifically, for most bouts of movement (i.e. angular velocity < 90 degrees), *C. reinhardtii* trajectories appear longer than those of *C. smithii* even when turning comparable amounts ([Figure 13](#)). These observations suggest that *C. reinhardtii* and *C. smithii* gametes employ qualitatively different exploratory strategies and display species-specific features of movement.

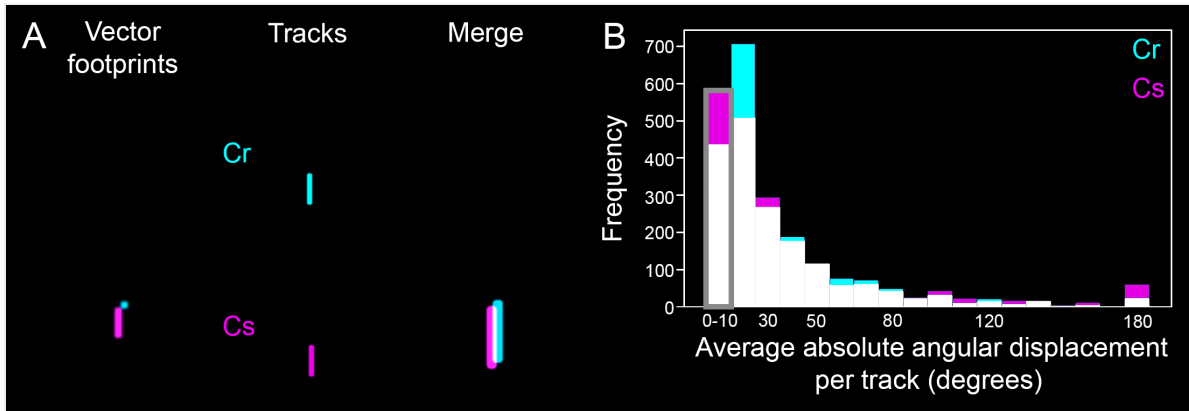


Figure 13

Motility tracks binned by average angular displacement show differences in swimming behavior between species.

(A) Merged images show the higher linear velocity of *C. reinhardtii* compared to *C. smithii*. Cr = *C. reinhardtii*. Cs = *C. smithii*. The “Tracks” and “Merge” panels show cumulative average projections of tracks, with Cr in cyan and Cs in magenta.

(B) We generated tracks of cell movement from vectors representing the frame-to-frame displacement of cells and then binned by the average absolute frame-to-frame angular displacement.

As the video plays, the grey box in (B) pans over bins to match the visual representations in (A).

We decided to quantify these apparent differences. To begin, we calculated the linear and angular velocities of individual cells from each species ([Figure 14, A](#)). We found significant differences between the species’ velocity distributions ([Figure 14, B](#)). On average, *C. reinhardtii* cells swim ~20 $\mu\text{m/s}$ faster than *C. smithii* cells and, overall,

display significantly greater velocities even in light of experimental variation (Figure 14, B). On the other hand, there is no difference in the distribution of mean angular velocity between these species (Figure 14, C). These findings support our qualitative observations that *C. reinhardtii* and *C. smithii* differ in the speed with which they explore a confined space.

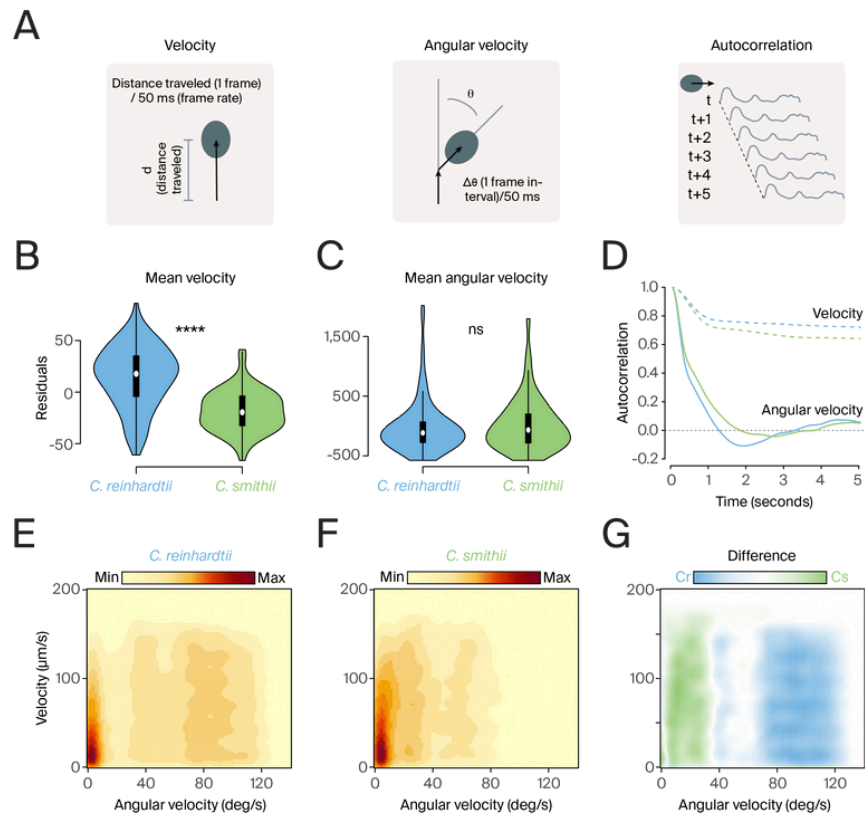


Figure 14

2D motility measurements for each species determined from video data of swimming cells, with each cell confined in an individual pool.

(A) Schematics show the different measures shown below: velocity, angular velocity, and autocorrelation.

(B–C) Violin plots comparing mean velocity as a function of species (Cr or Cs) and (C) mean angular velocity. The residuals are plotted after performing a linear regression that includes experiment (including all four replicates) as predictor. We used a Kruskal-Wallis test to determine the difference and the output was as follows: mean velocity ($\chi^2 = 73.633$, $df = 1$, $p < 0.0001$); mean angular velocity ($\chi^2 = 0.90868$, $df = 1$, $p = ns$), where **** $p < 0.0001$, ns = not significant.

(D) Autocorrelation distributions of velocity (dotted line) and angular velocity (solid line) for Cr (blue) and Cs (green). We

calculated autocorrelations over a five-second window. Autocorrelation values of 0 are represented by a dashed grey line.

(E–F) Probability density function representing the joint distribution of velocity and angular velocity for *C. reinhardtii* (E) or *C. smithii* (F). Darker colors correspond to a higher probability of occurrence.

(G) The difference between the joint distributions of angular velocity and velocity for *C. reinhardtii* (Figure 10, E) and *C. smithii* (Figure 10, F). Colors correspond to species bias; more blue represents a bias toward *C. reinhardtii* while more green corresponds to *C. smithii*.

The high-level differences in exploratory behavior we noted seemed to suggest variation in both speed *and* the rate of turning. Might apparent differences be better reflected in other representations of these motility features? We hypothesized that velocity and angular velocity might vary over time. To assess this, we analyzed the autocorrelations of velocity and angular velocity for each species over five-second windows (Figure 14, A). We found that the velocity of *C. reinhardtii* is more correlated over time, while its angular velocity autocorrelation decays faster than *C. smithii* (Figure 14, D). This means that it's easy to predict how fast *C. reinhardtii* will be swimming ~five seconds in the future, but it potentially executes turns more frequently and/or in a more variable fashion (Figure 14, D). Therefore, it appears that temporal variation in velocity parameters is an important feature delineating the motility patterns of *C. reinhardtii* and *C. smithii*.

In addition to temporal differences, autocorrelation analyses also suggest that each species is associated with unique combinations of angular velocity and velocity. Joint distributions of these two measures strongly supports this idea (Figure 14, E–G). Specifically, *C. reinhardtii* displays a greater range of velocities at which it executes high-degree turns (Figure 14, E, G). This observation corroborates the longer paths it displayed in our analyses of angular trajectories in (Figure 13). On the other hand, *C. smithii* was associated with more low-angle turns and a greater distribution of periods of time spent at low velocities (Figure 14, F, G).

Differences in cell swimming behavior: Multiple-cell swimming

Given the nature of our microchamber preparation, a percentage of wells contained more than one cell. We wondered if swimming behavior changes in the presence of multiple cells as compared to the behavior of solitary cells. To explore this, we repeated the same analyses as described above for single-cell data, but this time focused on wells in which more than one cell was present.

Comparing velocity distributions, we found roughly the same results as before: *C. reinhardtii* swims faster (though slightly less so in this instance), but the species do not differ in mean angular velocity ([Figure 15, A–B](#)). Notably, however, the autocorrelations of velocity and angular velocity are drastically different in the context of multiple cells. Autocorrelation distributions for each species displayed much more rapid decay when multiple cells were present ([Figure 15, C](#)), suggesting less predictable motility patterns and potentially more frequent switching between types of movement. There was also a corresponding shift in the joint distributions between angular velocity and velocity ([Figure 15, D–F](#)). *C. reinhardtii* executes much less high-velocity movement and spends much more time turning ([Figure 15, D](#)), while *C. smithii* responds to being close to multiple cells in an almost opposing fashion, relying on straight bouts of swimming and a lack of high-angle turns ([Figure 15, E](#)).

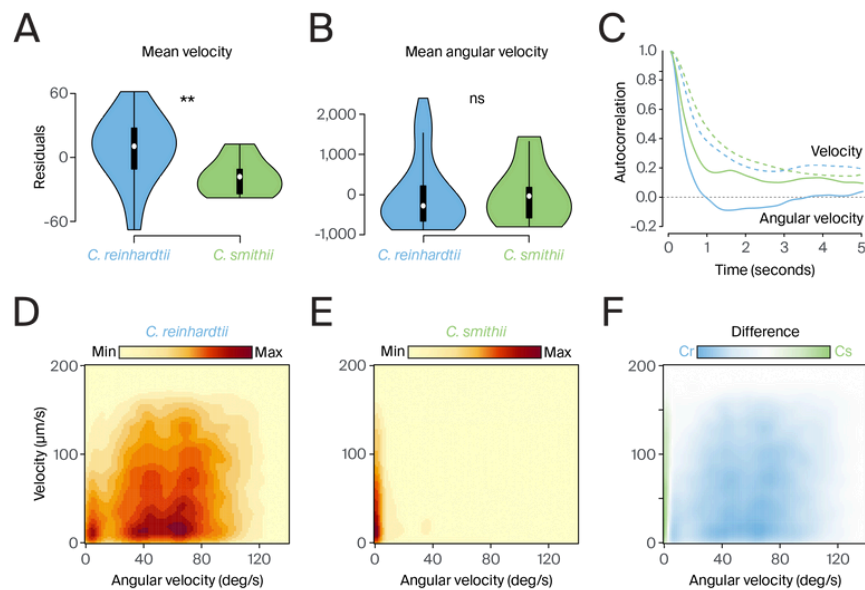


Figure 15

2D motility measurements for each species determined from video data of swimming cells, with multiple cells together in a single pool.

(A, B) Violin plots comparing multiple-cell measurements as a function of species (Cr or Cs), for (A) mean velocity and (B) mean angular velocity. The residuals are plotted after performing a linear regression that includes experiment (including all four replicates) as predictor. We used a Kruskal-Wallis test to determine the difference as follows: mean velocity ($X^2 = 9.145$, $df = 1$, $p < 0.01$); mean angular velocity ($X^2 = 0.026515$, $df = 1$, $p = ns$) where $**p < 0.01$, $ns =$ not significant.

(C) Autocorrelation distributions of velocity (dotted line) and angular velocity (solid line) for Cr (blue) and Cs (green) as in Figure 10D. Here, autocorrelations were calculated over five-second windows for trials in which more than one cell was present in a well. Autocorrelation values of 0 are represented by a dashed grey line.

(D) Probability density function representing the joint distribution of velocity and angular velocity for *C. reinhardtii*

for trials in which more than one cell was present. Darker colors correspond to a higher probability of occurrence.

(E) Probability density function representing the joint distribution of velocity and angular velocity for *C. smithii* for trials in which more than one cell was present. Darker colors correspond to a higher probability of occurrence.

(F) The difference between the joint distributions of angular velocity and velocity for *C. reinhardtii* (Figure 11, D) and *C. smithii* (Figure 11, E) for trials in which more than one cell was present. Colors correspond to species bias; more blue represents a bias toward *C. reinhardtii* while more green corresponds to *C. smithii*.

Visualizing organelle morphology

We suspect that for specific strains of progeny, we may want to perform higher-resolution imaging to study the subcellular morphology of *Chlamydomonas*. To accomplish that and avoid fixing the cells (a destructive technique), we adapted a method to keep the cells alive but immobilized such that we could obtain three-dimensional stacks of images using confocal microscopy [47]. We struggled to find cells that were positioned at the coverslip and fully immobile at first, so we're sharing a protocol to make this easier for others.

The step-by-step **protocol** we used to [immobilize cells for live imaging](#) is available on protocols.io.

Our previous reports of cell morphology measurements were done on more cells (four replicate experiments with 30 cells in each), but at lower resolution (imaged with a 10× objective), which is the higher-throughput approach that we will employ for characterizing many of the progeny strains from our cross. Here, we performed this experiment once (on 30 cells for each species) and imaged at a higher resolution (100×/1.45 NA objective and 2.8× SoRa) (Figure 16), which is a much lower-throughput method that we may only end up using for a select few strains. For the representative

images shown in [Figure 16](#), we've uploaded the raw and deconvolved data to [Zenodo](#) and shared the code for the Fiji macros on [GitHub](#). This processing workflow qualitatively increased the signal-to-noise ratio in our images and we'll use it for fluorescent imaging that requires this level of resolution going forward.

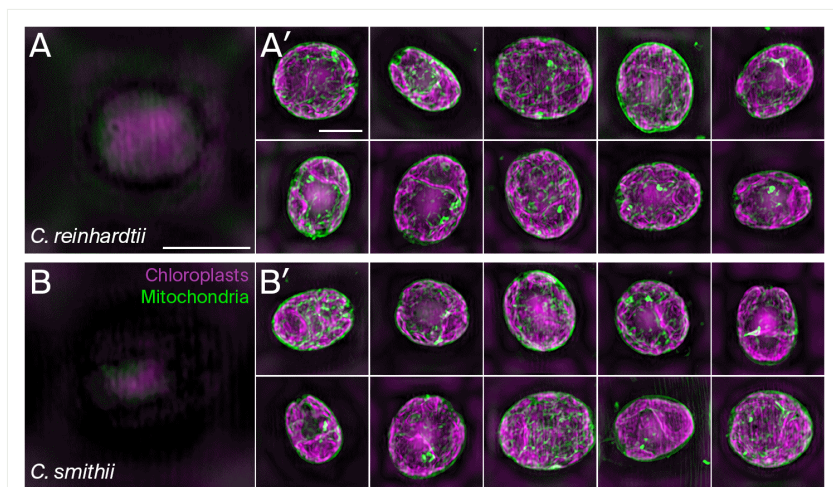


Figure 16

Representative images show *Chlamydomonas* sp. chloroplast and mitochondria organelle morphology.

(A, B) Representative optical sectioning through z (100-nm step size).

(A', B') Maximum intensity projections (MIPs) of representative data from *Chlamydomonas reinhardtii* (A, A') and *C. smithii* (B, B'). The top-left MIP for each species is represented by the Z-stack animation shown in A and B. Chloroplast localization is shown in magenta (autofluorescence, ex. 640 nm) and the mitochondrial localization is shown in green (stained by PKmito ORANGE, ex. 561 nm).

Scale bars: 5 μm

In future work, we'll explore different methods to segment and quantify the organelles. We'll compare traditional segmentation approaches that rely on human judgment to

deep-learning methods for denoising and segmenting these images to find an approach that allows us to reproducibly quantify the organelle volumes. If we find robust differences in the volumes of organelles (chloroplasts and mitochondria) between the parent species, we'll characterize the progeny with this workflow.

Key takeaways

Chlamydomonas reinhardtii and *smithii* were isolated in the same year under similar conditions and maintained through continuous subculturing, but we have observed clear differences between the two species:

- *C. smithii* is more adaptable to various growth media ranging from water to nutrient-rich media.
- *C. smithii* takes on a unique morphology when grown on marine broth with L1 nutrients.
- *C. smithii* is slightly more sensitive to harsh antibiotic cocktails.
- *C. smithii* is more easily lysed in detergent.
- *C. reinhardtii* appears to have a thicker cell wall.
- *C. smithii* is more sensitive to magnetic fields.
- *C. smithii* is 21% larger than *C. reinhardtii* and more oblong.
- Extracting the frames where a swimming cell is in focus reduces data processing time and increases the accuracy of morphology measurements.
- *C. reinhardtii* and *C. smithii* differ qualitatively in how they explore during confinement.
- Exploratory differences between the two species are associated with complex patterns of motility that vary over time.
- The motility patterns displayed by *C. reinhardtii* and *C. smithii* gametes diverge when gametes are confined with other cells.

Next steps

Our ultimate goal is to find a set of traits that differ quantitatively between *C. reinhardtii* and *C. smithii* so we can compare the phenotypes of their progeny back to the parent species. We're working to assess other phenotypes in addition to those we have reported here, including growth curves in liquid media, chloroplast fluorescence decay, flagellar beating rates, and phototaxis assays. We'll share any additional phenotypic data in new pubs.

In addition to identifying useful phenotypes, we're developing novel techniques to quantify them in a high-quality, high-throughput manner. We're also working on high-throughput genotyping methods so that we can thoroughly map genotype-phenotype linkages of the recombinant progeny.

In the future, we're interested in applying existing deep-learning approaches to better segment and quantify our fluorescent image data.

References

- 1 Niepoth N, Bendesky A. (2020). How Natural Genetic Variation Shapes Behavior. <https://doi.org/10.1146/annurev-genom-111219-080427>
- 2 Bell RA, Cain JR. (1983). Sexual reproduction and hybridization in *Chlamydomonas smithii* and *C. reinhardtii* (Chlorophyceae, Volvocales). <https://doi.org/10.2216/i0031-8884-22-3-243.1>
- 3 Hoshaw RW, Ettl H. (1966). *CHLAMYDOMONAS SMITHII* SP. NOV.—A *CHLAMYDOMONAD* INTERFERTILE WITH *CHLAMYDOMONAS REINHARDTII*. <https://doi.org/10.1111/j.1529-8817.1966.tb04600.x>
- 4 Harris EH. (2001). *Chlamydomonas* as a Model Organism. <https://doi.org/10.1146/annurev.arplant.52.1.363>
- 5 Pröschold T, Harris EH, Coleman AW. (2005). Portrait of a Species. <https://doi.org/10.1534/genetics.105.044503>

- 6 Harris EH. (1989). An Overview of the Genus *Chlamydomonas*.
<https://doi.org/10.1016/b978-0-12-326880-8.50006-7>
- 7 Flowers JM, Hazzouri KM, Pham GM, Rosas U, Bahmani T, Khraiwesh B, Nelson DR, Jijakli K, Abdrabu R, Harris EH, Lefebvre PA, Hom EFY, Salehi-Ashtiani K, Purugganan MD. (2015). Whole-Genome Resequencing Reveals Extensive Natural Variation in the Model Green Alga *Chlamydomonas reinhardtii*.
<https://doi.org/10.1105/tpc.15.00492>
- 8 Boynton JE, Harris EH, Burkhart BD, Lamerson PM, Gillham NW. (1987). Transmission of mitochondrial and chloroplast genomes in crosses of *Chlamydomonas*. <https://doi.org/10.1073/pnas.84.8.2391>
- 9 Nakamura S. (2010). Paternal inheritance of mitochondria in *Chlamydomonas*.
<https://doi.org/10.1007/s10265-009-0295-8>
- 10 Colleaux L, Michel-Wolwertz M-R, Matagne RF, Dujon B. (1990). The apocytochrome b gene of *Chlamydomonas smithii* contains a mobile intron related to both *Saccharomyces* and *Neurospora* introns.
<https://doi.org/10.1007/bf00265065>
- 11 Remacle C, Bovie C, Michel-Wolwertz M-R, Loppes R, Matagne RF. (1990). Mitochondrial genome transmission in *Chlamydomonas* diploids obtained by sexual crosses and artificial fusions: Role of the mating type and of a 1 kb intron.
<https://doi.org/10.1007/bf00265051>
- 12 Buchberger F, Stibor H, Neusius D, Nickelsen J, Stockenreiter M. (2019). Transgenic and cell wall-deficient *Chlamydomonas reinhardtii* food affects life history of *Daphnia magna*. <https://doi.org/10.1007/s10811-019-01983-7>
- 13 Matagne RF, Michel-Wolwertz M-R, Dombrowicz D. (1987). Artificially induced fusions between *Chlamydomonas reinhardtii* and *Chlamydomonas smithii*. Transmission of non-mendelian traits in the fusion products.
[https://doi.org/10.1016/0168-9452\(87\)90107-5](https://doi.org/10.1016/0168-9452(87)90107-5)
- 14 Rochaix J-D. (2013). *Chlamydomonas reinhardtii*. <https://doi.org/10.1016/b978-0-12-374984-0.00230-8>
- 15 Davies DR, Plaskitt A. (1971). Genetical and structural analyses of cell-wall formation in *Chlamydomonas reinhardtii*.
<https://doi.org/10.1017/s0016672300012015>
- 16 Rohatgi A. (2022). Webplotdigitizer: Version 4.6.
<https://automeris.io/WebPlotDigitizer>

- 17 JONES GE. (1967). PRECIPITATES FROM AUTOCLAVED SEAWATER1. <https://doi.org/10.4319/lo.1967.12.1.0165>
- 18 Zobell CE. (1941). Studies on marine bacteria. I. The cultural requirements of heterotrophic aerobes. https://elischolar.library.yale.edu/cgi/viewcontent.cgi?article=1581&context=journal_of_marine_research
- 19 Avasthi P, Essock-Burns T, Garcia G, Gehring J, Matus DQ, Mets DG, York R. (2024). Gotta catch 'em all: Agar microchambers for high-throughput single-cell live imaging. <https://doi.org/10.57844/ARCADIA-V1BG-6B60>
- 20 Essock-Burns T. (2023). Molding microchambers in agar with PDMS stamps for live imaging v1. <https://doi.org/10.17504/protocols.io.j8nlkwpk1l5r/v1>
- 21 Thevenaz P, Ruttimann UE, Unser M. (1998). A pyramid approach to subpixel registration based on intensity. <https://doi.org/10.1109/83.650848>
- 22 Bentley SA, Anagnostidis V, Schlogelhofer HL, Gielen F, Wan KY. (2021). Phenotyping single-cell motility in microfluidic confinement. <https://doi.org/10.1101/2021.12.24.474109>
- 23 Schindelin J, Arganda-Carreras I, Frise E, Kaynig V, Longair M, Pietzsch T, Preibisch S, Rueden C, Saalfeld S, Schmid B, Tinevez J-Y, White DJ, Hartenstein V, Eliceiri K, Tomancak P, Cardona A. (2012). Fiji: an open-source platform for biological-image analysis. <https://doi.org/10.1038/nmeth.2019>
- 24 Salido J, Sánchez C, Ruiz-Santaquiteria J, Cristóbal G, Blanco S, Bueno G. (2020). A Low-Cost Automated Digital Microscopy Platform for Automatic Identification of Diatoms. <https://doi.org/10.3390/app10176033>
- 25 Berg S, Kutra D, Kroeger T, Straehle CN, Kausler BX, Haubold C, Schiegg M, Ales J, Beier T, Rudy M, Eren K, Cervantes JI, Xu B, Beuttenmueller F, Wolny A, Zhang C, Koethe U, Hamprecht FA, Kreshuk A. (2019). ilastik: interactive machine learning for (bio)image analysis. <https://doi.org/10.1038/s41592-019-0582-9>
- 26 Stirling DR, Swain-Bowden MJ, Lucas AM, Carpenter AE, Cimini BA, Goodman A. (2021). CellProfiler 4: improvements in speed, utility and usability. <https://doi.org/10.1186/s12859-021-04344-9>
- 27 Sage D, Donati L, Soulez F, Fortun D, Schmit G, Seitz A, Guet R, Vonesch C, Unser M. (2017). DeconvolutionLab2: An open-source software for deconvolution microscopy. <https://doi.org/10.1016/j.jymeth.2016.12.015>
- 28 Glaesener AG, Merchant SS, Blaby-Haas CE. (2013). Iron economy in *Chlamydomonas reinhardtii*. <https://doi.org/10.3389/fpls.2013.00337>

- 29 Vítová M, Bišová K, Hlavová M, Kawano S, Zachleder V, Čížková M. (2011). *Chlamydomonas reinhardtii*: duration of its cell cycle and phases at growth rates affected by temperature. <https://doi.org/10.1007/s00425-011-1427-7>
- 30 Guillard RRL. (1975). Culture of Phytoplankton for Feeding Marine Invertebrates. https://doi.org/10.1007/978-1-4615-8714-9_3
- 31 UNESCO. (2003). Manual on Harmful Marine Microalgae
- 32 Keller MD, Selvin RC, Claus W, Guillard RRL. (1987). MEDIA FOR THE CULTURE OF OCEANIC ULTRAPHYTOPLANKTON^{1,2}. <https://doi.org/10.1111/j.1529-8817.1987.tb04217.x>
- 33 Shetty P, Gitau MM, Maróti G. (2019). Salinity Stress Responses and Adaptation Mechanisms in Eukaryotic Green Microalgae. <https://doi.org/10.3390/cells8121657>
- 34 Hellebust JA, Le Gresley SML. (1985). Growth characteristics of the marine rock pool flagellate *Chlamydomonas pulsatilla* Wollenweber (Chlorophyta). <https://doi.org/10.2216/i0031-8884-24-2-225.1>
- 35 Čížková M, Slavková M, Vítová M, Zachleder V, Bišová K. (2019). Response of the Green Alga *Chlamydomonas reinhardtii* to the DNA Damaging Agent Zeocin. <https://doi.org/10.3390/cells8070735>
- 36 Kan Y, Pan J. (2010). A ONE-SHOT SOLUTION TO BACTERIAL AND FUNGAL CONTAMINATION IN THE GREEN ALGA *CHLAMYDOMONAS REINHARDTII* CULTURE BY USING AN ANTIBIOTIC COCKTAIL¹. <https://doi.org/10.1111/j.1529-8817.2010.00904.x>
- 37 Vela GR, Rosenthal RS. (1972). Effect of Peptone on *Azotobacter* Morphology. <https://doi.org/10.1128/jb.111.1.260-266.1972>
- 38 Hwang H-J, Kim YT, Kang NS, Han JW. (2018). A Simple Method for Removal of the *Chlamydomonas reinhardtii* Cell Wall Using a Commercially Available Subtilisin (Alcalase). <https://doi.org/10.1159/000495183>
- 39 Herth W, Schnepf E. (1980). The fluorochrome, calcofluor white, binds oriented to structural polysaccharide fibrils. <https://doi.org/10.1007/bf01279855>
- 40 Ram AFJ, Klis FM. (2006). Identification of fungal cell wall mutants using susceptibility assays based on Calcofluor white and Congo red. <https://doi.org/10.1038/nprot.2006.397>
- 41 Roncero C, Durán A. (1985). Effect of Calcofluor white and Congo red on fungal cell wall morphogenesis: in vivo activation of chitin polymerization.

<https://doi.org/10.1128/jb.163.3.1180-1185.1985>

- 42 Hernández-Zamora M, Perales-Vela HV, Flores-Ortíz CM, Cañizares-Villanueva RO. (2014). Physiological and biochemical responses of *Chlorella vulgaris* to Congo red. <https://doi.org/10.1016/j.ecoenv.2014.05.030>
 - 43 Hernández-Zamora M, Martínez-Jerónimo F. (2019). Congo red dye diversely affects organisms of different trophic levels: a comparative study with microalgae, cladocerans, and zebrafish embryos. <https://doi.org/10.1007/s11356-019-04589-1>
 - 44 Tyurin AA, Suhorukova AV, Deineko IV, Pavlenko OS, Fridman VA, Goldenkova-Pavlova IV. (2021). A high throughput assay of lichenase activity with Congo red dye in plants. <https://doi.org/10.1186/s13007-021-00801-x>
 - 45 Bauer LM, da Gloria Esquivel M, Costa JAV, da Rosa APC, Santos LO. (2023). Influence of Cell Wall on Biomolecules Biosynthesis in *Chlamydomonas reinhardtii* Strains Exposed to Magnetic Fields. <https://doi.org/10.1007/s00284-023-03189-0>
 - 46 Celebi FM, Cheveralls K, Chou S, Essock-Burns T, Garcia G. (2024). Streamlining microscopy datasets by enriching for in-focus frames. <https://doi.org/10.57844/ARCADIA-D86F-498C>
 - 47 Iwai M, Roth MS, Niyogi KK. (2018). Subdiffraction-resolution live-cell imaging for visualizing thylakoid membranes. <https://doi.org/10.1111/tpj.14021>
-